

# EXPLOSIVE NUCLEOSYNTHESIS IN THE NEUTRINO-DRIVEN ASPHERICAL SUPERNOVA EXPLOSION OF A NON-ROTATING $15M_{\odot}$ STAR WITH SOLAR METALLICITY

SHIN-ICHIRO FUJIMOTO<sup>1</sup>, KEI KOTAKE<sup>2</sup>, MASA-AKI HASHIMOTO<sup>3</sup>, MASAOMI ONO<sup>3</sup>, AND NAOFUMI OHNISHI<sup>4</sup>

*Accepted in Astrophys. J.*

## ABSTRACT

We investigate explosive nucleosynthesis in a non-rotating  $15M_{\odot}$  star with solar metallicity that explodes by a neutrino-heating supernova (SN) mechanism aided by both standing accretion shock instability (SASI) and convection. To trigger explosions in our two-dimensional hydrodynamic simulations, we approximate the neutrino transport with a simple light-bulb scheme and systematically change the neutrino fluxes emitted from the protoneutron star. By a post-processing calculation, we evaluate abundances and masses of the SN ejecta for nuclei with the mass number  $\leq 70$  employing a large nuclear reaction network. Aspherical abundance distributions, which are observed in nearby core-collapse SN remnants, are obtained for the non-rotating spherically-symmetric progenitor, due to the growth of low-mode SASI. Abundance pattern of the supernova ejecta is similar to that of the solar system for models whose masses ranges  $(0.4-0.5)M_{\odot}$  of the ejecta from the inner region ( $\leq 10,000$  km) of the precollapse core. For the models, the explosion energies and the  $^{56}\text{Ni}$  masses are  $\simeq 10^{51}$  erg and  $(0.05-0.06)M_{\odot}$ , respectively; their estimated baryonic masses of the neutron star are comparable to the ones observed in neutron-star binaries. These findings may have little uncertainty because most of the ejecta is composed by matter that is heated via the shock wave and has relatively definite abundances. The abundance ratios for Ne, Mg, Si and Fe observed in Cygnus loop are well reproduced with the SN ejecta from an inner region of the  $15M_{\odot}$  progenitor.

*Subject headings:* Nuclear reactions, nucleosynthesis, abundances — stars: supernovae: general — Hydrodynamics — Methods: numerical

## 1. INTRODUCTION

The explosion mechanism of core-collapse supernovae (SNe) is still not clearly understood. Multi-dimensional effects such as standing accretion shock instability (SASI) and convection are recognized to be most important for unveiling the explosion mechanism, in particular for a progenitor heavier than about  $11M_{\odot}$  in its main sequence phase (Kitaura et al. 2006; Buras et al. 2006a,b). Here SASI, becoming very popular in current supernova researches, is a uni- and bipolar sloshing of the stalled supernova shock with pulsational strong expansion and contraction (see, e.g., Blondin et al. (2003); Scheck et al. (2004); Ohnishi et al. (2006); Foglizzo et al. (2007); Blondin & Mezzacappa (2007); Iwakami et al. (2008, 2009); Nordhaus et al. (2010) and references therein). Some of recent two-dimensional (2D) radiation-hydrodynamic simulations show that the delayed neutrino-driven mechanism aided by SASI and convection does work to produce aspherical explosions (Marek et al. 2009; Marek & Janka 2009; Suwa et al. 2010).

Observationally, global anisotropies and mixing as well as smaller-scale clumping of the SN ejecta, are common features of SN remnants like in SN1987A (Wang et al. 2002), Cas A (Hughes et al. 2000; Willingale et al. 2002), G292.0+1.8 (Park et al. 2007), and Cygnus loop (Kimura 2009; Uchida et al. 2009). Asymmetries commonly observed in the nebular emission-line profiles are considered as an

evidence that core-collapse SNe occur generally aspherically (Maeda et al. 2008; Modjaz et al. 2008; Tanaka et al. 2009b; Taubenberger et al. 2009). Evidences for asymmetry are also obtained from spectropolarimetric observations of Type Ibc SN at an early phase ( $\sim$  days) (see, e.g., Tanaka et al. (2008, 2009a) and references therein).

Thus far, nucleosynthesis studies of the SN ejecta have almost successfully reproduced the solar composition and abundances of radioactives observed in SN1987A (Hashimoto 1995; Woosley & Weaver 1995; Thielemann et al. 1996; Rauscher et al. 2002). However those spherical models have some problems such as overproduction of neutron-rich Ni isotopes and underproductions of  $^{44}\text{Ti}$ ,  $^{64}\text{Zn}$  and light  $p$ -nuclei (Rauscher et al. 2002).

Aspherical effects on the explosive nucleosynthesis have been investigated by Nagataki et al. (1997); Nagataki (2000). Based on 2D hydrodynamic simulations in which the explosion was triggered by some form of manual energy deposition into a stellar progenitor model outside the so-called mass cut, they evaluated the composition of the ejecta with a large nuclear reaction network. They pointed out that  $^{44}\text{Ti}$  can be produced more abundantly in the case of jet-like explosions compared to that of spherical explosions. Young et al. (2006) examined the composition of the ejecta in three-dimensional (3D) SPH simulations to discuss a candidate of the progenitor of Cas A. They showed that the abundances of  $^{56}\text{Ni}$  and  $^{44}\text{Ti}$  depend on the magnitude and asymmetry of the explosion energy as well as on the amount of the fallback. The effects of the fallback on the abundances have been systematically studied in one-dimensional explosion models (Young & Fryer 2007). More recently, 3D effects have been more elaborately studied (Hungerford et al. 2003, 2005), as well as the impacts of different explosions by employing a number of progenitors (Joggerst et al. 2009, 2010) or by assum-

<sup>1</sup> Kumamoto National College of Technology, 2659-2 Suya, Goshi, Kumamoto 861-1102, Japan; fujimoto@ec.knct.ac.jp.

<sup>2</sup> Division of Theoretical Astronomy, National Astronomical Observatory Japan, 2-21-1, Osawa, Mitaka, Tokyo, 181-8588, Japan.

<sup>3</sup> Department of Physics, School of Sciences, Kyushu University, Fukuoka 810-8560, Japan.

<sup>4</sup> Department of Aerospace Engineering, Tohoku University, 6-6-01 Aramaki-Aza-Aoba, Aoba-ku, Sendai, 980-8579, Japan.

ing a jet-like explosion (Couch et al. 2009; Tominaga 2009), which is one of the possible candidates of hypernovae (e.g., Maeda & Nomoto (2003); Nagataki et al. (2006)).

In addition to the above-mentioned work, nucleosynthesis in a more realistic simulation that models the multidimensional neutrino-driven SN explosion has been also extensively studied (Kifonidis et al. 2003, 2006; Gawryszczak et al. 2010). Although a small network has ever been included in the computations, these 2D simulations employing a light-bulb scheme (Kifonidis et al. 2003) or a more accurate gray transport scheme (Scheck et al. 2006; Kifonidis et al. 2006) have made it possible to elucidate the nucleosynthesis inside from the iron core after the shock-revival up to explosion in a more consistent manner. Kifonidis et al. (2006) demonstrated that the SASI-aided low-mode explosions can most naturally explain the masses and distribution of the synthesized elements observed in SN1987A. Their recent 3D results by Hammer et al. (2010) show that the 3D effects that affect the velocity of the ejecta as well as the growth of the Rayleigh-Taylor instability are really important to correctly determine the properties of the ejecta.

In the present work, we study explosive nucleosynthesis in a non-rotating  $15 M_{\odot}$  star with solar metallicity by performing 2D hydrodynamic simulations that models a SASI-aided delayed explosion via a light-bulb scheme. To extract a detailed information of the synthesized elements, we follow the abundance evolution by employing a large nuclear reaction network. It should be emphasized that the mass cut as well as the aspherical distribution of the explosion energy are evaluated from the hydrodynamic simulations, as in our previous work on the nucleosynthesis in magnetohydrodynamically-driven SN explosions (Nishimura et al. 2006) as well as in collapsars (Fujimoto et al. 2007, 2008; Ono et al. 2009).

In §2, this paper opens up with a brief description of a numerical code for the hydrodynamic calculation, initial conditions of the progenitor star, and properties of the aspherical explosion. In §3, we present a large nuclear reaction network, physical properties of SN ejecta, and abundances and masses of the ejecta, and heavy-nuclei distribution of the SN ejecta. We discuss the uncertainty in the estimate of the abundances and masses and compare the evaluated abundances with those observed in Cygnus loop in §4. Finally we will summarize our results in §5.

## 2. HYDRODYNAMIC SIMULATIONS OF AN ASPHERICAL NEUTRINO-DRIVEN SUPERNOVA EXPLOSION

### 2.1. Hydrodynamic code and initial conditions

To calculate the structure and evolution of the collapsing star, we solve the Newtonian hydrodynamic equations,

$$\frac{D\rho}{Dt} + \rho \nabla \cdot \mathbf{v} = 0, \quad (1)$$

$$\rho \frac{D\mathbf{v}}{Dt} = -\nabla P - \rho \nabla (\Phi + \Phi_c) \quad (2)$$

$$\rho \frac{d}{dt} \left( \frac{e}{\rho} \right) = -P \nabla \cdot \mathbf{v} + Q_E, \quad (3)$$

$$\frac{DY_e}{Dt} = Q_N, \quad (4)$$

where  $\rho$ ,  $P$ ,  $\mathbf{v}$ ,  $e$ , and  $Y_e$ , are the mass density, the pressure the fluid velocity, the internal energy density, and the electron fraction, respectively. We denote the Lagrange derivative as

$D/Dt$ . The gravitational potential of fluid and the central object with a mass of  $M_{\text{in}}$ ,  $\Phi$  and  $\Phi_c$ , are evaluated with

$$\Delta \Phi = 4\pi G \rho, \quad (5)$$

and

$$\Phi_c = -\frac{GM_{\text{in}}}{r}, \quad (6)$$

where  $G$  is the gravitational constant. We note that  $M_{\text{in}}$  continuously increases due to mass accretion through the inner boundary.

$Q_E$  and  $Q_N$  are the source terms that describe the rate of change per unit volume in equations (3) and (4), respectively, and will be summarized in Appendix A and B. In the present study, we take into account absorption of electron and anti-electron neutrinos as well as neutrino emission through electron and positron captures, electron-positron pair annihilation, nucleon-nucleon bremsstrahlung, and plasmon-decays. We assume that the fluid is axisymmetric and that neutrinos are isotropically emitted from the neutrino spheres with given luminosities and with the Fermi-Dirac distribution of given temperatures (Ohnishi et al. 2006). Rates for absorption of neutrinos and neutrino emission through electron and positron captures are taken from Scheck et al. (2006, appendix D). Geometrical factor  $f_\nu$  is set to be

$$f_\nu = \frac{1}{2} \left[ 1 + \sqrt{1 - (R_\nu/r)^2} \right], \quad (7)$$

as in Scheck et al. (2006). Here  $R_\nu$  is the radius of neutrino sphere and is simply estimated with the relation,  $L_\nu = \frac{7}{16} \sigma T_\nu^4 \cdot 4\pi R_\nu^2$  for a given set of the luminosity  $L_\nu$  and temperature  $T_\nu$  (Ohnishi et al. 2006), where  $\sigma$  is the Stefan-Boltzmann constant. We adopt rates for the emission of neutrinos ( $\nu_e, \bar{\nu}_e, \nu_x, \bar{\nu}_x$ ) through pair annihilation, bremsstrahlung, and plasmon-decays as in Ruffert et al. (1996, Appendix B). Moreover, we include the heating term in  $Q_E$  due to the absorption of neutrinos on  $^4\text{He}$  and the inelastic scatterings on  $^4\text{He}$  via neutral currents (Haxton 1988; Ohnishi et al. 2007).

The numerical code for the hydrodynamic calculations employed in this paper is based on the ZEUS-2D code (Stone & Norman 1992; Ohnishi et al. 2006). We use a realistic equation of state (EOS) based on the relativistic mean field theory (Shen et al. 1998). For lower density regime ( $\rho < 10^5 \text{ g/cm}^3$ ), where no data is available in the EOS table with the Shen EOS, we use another EOS, which includes contributions from an ideal gas of nuclei, radiation, and electrons and positrons with arbitrary degrees of degeneracy (Blinnikov et al. 1996). We carefully connect two EOS at  $\rho = 10^5 \text{ g/cm}^3$  for physical quantities to vary continuous in density at a given temperature (Fujimoto et al. 2006).

First we perform a spherical symmetric hydrodynamic simulation of the core collapse of a  $15M_{\odot}$  non-rotating star with the solar metallicity (Woosley & Weaver 1995) using a hydrodynamic code (Kotake et al. 2004) for about 10 ms after core-bounce, when the bounce shock turns into a standing accretion shock and the proto neutron star (PNS) grows to  $\sim 1.2M_{\odot}$ . Then, we map distributions of densities, temperatures, radial velocities and electron fractions of the spherical symmetric simulation to initial distribution for two-dimensional (2D) hydrodynamic simulations. After the remap, the central region inside 50 km in radius is excised to follow a long-term post-bounce evolution (e.g., Scheck et al. (2006); Kifonidis et al. (2006)). We impose velocity perturbations to the unperturbed radial velocity in a dipolar manner, and follow the postbounce

evolution. The spherical coordinates are used in our simulations and the computational domain is extended over  $50\text{ km} \leq r \leq 50,000\text{ km}$  and  $0 \leq \theta \leq \pi$ , or from the Fe core to inner O-rich layers, which are covered with  $500(r) \times 128(\theta)$  meshes. The mass is  $3.17M_\odot$  in the computational domain. We note that convective motion occurs at the onset of the 2D simulation with the above meshes, while the motion does not appear in the case of coarser mesh points of  $500(r) \times 60(\theta)$ . Evolution of the explosion energy and mass ejection rate are very similar to those for high resolution simulation with  $300(r) \times 196(\theta)$  meshes ( $50\text{ km} \leq r \leq 3,000\text{ km}$  and  $0 \leq \theta \leq \pi$ ) for about 350 ms after the core bounce. Therefore resolution of the simulations with  $500(r) \times 128(\theta)$  meshes seems to be appropriate for the present study. However the resolution may be too low to follow later time evolution of the explosion towards homologous expansion (Gawryszczak et al. 2010). For the high resolution simulation, the minimum grid size in the radial- and lateral( $\theta$ )-directions,  $\delta r$  and  $\delta\theta$ , is 1 km and  $\pi/196$ , respectively, while  $\delta r = 1\text{ km}$  and  $\delta\theta = \pi/128$  for our fiducial set (i.e.,  $500(r) \times 128(\theta)$  mesh points).

## 2.2. Aspherical SN explosion

We have performed the simulations for models with the electron-neutrino luminosities,  $L_{\nu_e} = 3.7, 3.9, 4.0, 4.2, 4.5, 4.7$ , and  $5.0 \times 10^{52}\text{ erg s}^{-1}$  for 1–2 s after the core bounce, when a shock front has reached to a layer with  $r = 10,000\text{ km}$  in almost all directions. We take the input neutrino luminosities as above because the revival of the stalled bounce shock occurs only for models with  $L_{\nu_e} \geq 3.9 \times 10^{52}\text{ erg s}^{-1}$ , and also because for models with  $L_{\nu_e} > 5.0 \times 10^{52}\text{ erg s}^{-1}$ , the star explodes too early for the SASI to grow, as will be discussed later. We set  $L_{\bar{\nu}_e} = L_{\nu_e}$  and  $L_{\nu_x} = 0.5L_{\nu_e}$ , where  $L_{\bar{\nu}_e}$  and  $L_{\nu_x}$  are the luminosities of anti-electron neutrino and other-types ( $\mu$ ,  $\tau$ , anti- $\mu$ , and anti- $\tau$ ), respectively. We consider models with neutrino temperatures,  $T_{\nu_e}$ ,  $T_{\bar{\nu}_e}$ , and  $T_{\nu_x}$  as 4 MeV, 5 MeV, and 10 MeV, respectively (Ohnishi et al. 2006). The adopted neutrino luminosities are comparable to those with a more accurate transport scheme but the temperatures are slightly higher (Marek et al. 2009; Marek & Janka 2009). We will present hydrodynamic and nucleosynthetic results for cases with lower neutrino temperatures, in §4.1.

We confirm that the explosion are highly aspherical and  $l=1$  and  $l=2$  modes are dominant as shown in Kifonidis et al. (2006); Ohnishi et al. (2006); Scheck et al. (2006), although the shape of the explosion strongly depends on numerical detail, such as mesh resolution and boundary conditions (Kifonidis et al. 2006; Scheck et al. 2006). Entropy contour of the hydrodynamic simulation is shown in Figure 1 for case with  $L_{\nu_e} = 4.5 \times 10^{52}\text{ erg s}^{-1}$ . Most of SN ejecta have entropy less than  $20k_B$ , where  $k_B$  is the Boltzmann constant. Entropy attains to  $70k_B$  for small amounts of the ejecta.

We find that for models with  $L_{\nu_e} \geq 3.9 \times 10^{52}\text{ erg s}^{-1}$ , the star explodes aspherically via the neutrino heating aided by SASI. Figure 2(a) shows explosion energies as a function of  $L_{\nu_e}$ , for all the exploded models. The energies are estimated at an epoch of 500 ms after the explosion and slightly increase after the epoch. Kinetic and thermal energies of the explosion are also shown in Figure 2(a). The thermal energies dominate over the kinetic ones.

Higher  $L_{\nu_e}$  makes the onset of explosion earlier and also the mass of the PNS ( $M_{\text{pNS}}$ ) smaller. Note that we estimate  $M_{\text{pNS}}$  at  $t = t_{\text{exp}} + 500\text{ ms}$ , because  $M_{\text{pNS}}$  only slightly increases later than 500 ms after  $t_{\text{exp}}$ . Here  $t_{\text{exp}}$  indicates the time scale when the explosion sets in, which can be typically estimated

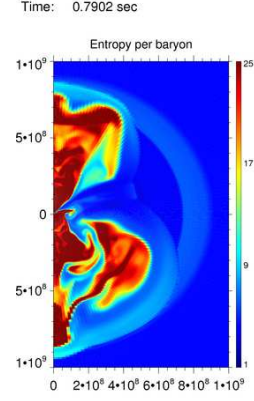


FIG. 1.— Entropy contour for case with  $L_{\nu_e} = 4.5 \times 10^{52}\text{ erg s}^{-1}$  at 0.79 s after the core bounce. The growth of low-mode SASI is prominent.

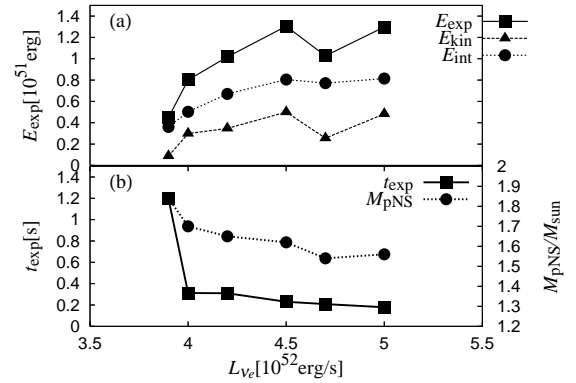


FIG. 2.— (a) Explosion energies vs. neutrino luminosities. Filled squares, circles, and triangles indicate explosion energies, kinetic-part and thermal-part of the explosion energies, respectively. (b)  $M_{\text{pNS}}$  and  $t_{\text{exp}}$  vs. neutrino luminosities. Filled squares and circles indicate  $t_{\text{exp}}$  and  $M_{\text{pNS}}$ , respectively.

when the mass ejection rate at  $100\text{ km}$  grows up  $0.1M_\odot\text{ s}^{-1}$  in our 2D simulations. Figure 2(b) shows the explosion time  $t_{\text{exp}}$  and  $M_{\text{pNS}}$  as a function of  $L_{\nu_e}$ . Except for the lowest luminosity model ( $L_{\nu_e} \leq 3.9 \times 10^{52}\text{ erg s}^{-1}$ ),  $M_{\text{pNS}}$  is in the range of  $1.54 - 1.70M_\odot$ . These values are much larger than the so-called mass-cut in the spherical model of  $15M_\odot$  progenitors by Hashimoto (1995) and Rauscher et al. (2002), which is  $1.30M_\odot$  and  $1.32M_\odot$ , respectively. The mass of the PNS however becomes larger ( $1.68M_\odot$ ) due to the fallback of ejecta (Rauscher et al. 2002).

## 3. NUCLEOSYNTHESIS IN SUPERNOVA EJECTA

### 3.1. Nuclear reaction network and initial composition

In order to calculate chemical composition of the SN ejecta, we need Lagrangian evolution of physical quantities, such as density, temperature, and, velocity of the material. We adopt a tracer particle method (Nagataki et al. 1997; Seitenzahl et al. 2010) to calculate the Lagrangian evolution of the physical quantities from the Eulerian evolution obtained from our simulations. The Lagrangian evolution is followed during the 2D aspherical simulation as well as the spherical collapsing phase. To get information on mass elements, 6,000 tracer particles are placed in the regions from 300 extending to 10,000 km (the O-rich layer). We have confirmed that the estimated energies and masses of the ejecta with the 6,000 particles are equal to the ones with 3,000 particles within  $\sim 1\%$  accuracy

and the obtained abundance profiles are also very similar.

Initial abundances of the particles are set to be those of the star just before the core collapse (Rauscher et al. 2002), in which 1400 nuclei are taken into account. We note that a presupernova model in Rauscher et al. (2002) has smaller helium, carbon-oxygen, and oxygen-neon core masses, compared with those in Woosley & Weaver (1995), due to coupled effects through the inclusion of mass loss and the revisions of opacity and nuclear inputs (Rauscher et al. 2002). The mass of a particle in a layer is weighted to the mass in the layer. We note that the minimum mass of the particles is  $\sim 10^{-4} M_{\odot}$ . We find that more than one fifth particles are ejected due to the aspherical explosion.

Next we calculate abundances and masses of the supernova ejecta. Ejecta that is located on the inner region of the star ( $r_{\text{ej,cc}} \leq 10,000 \text{ km}$ ) before the core collapse, has high maximum temperatures enough for elements heavier than C to burn explosively. Here  $r_{\text{ej,cc}}$  is the radius of the ejecta at the core collapse. We therefore follow abundance evolution of the ejecta from the inner region using a nuclear reaction network, which includes 463 nuclide from neutron, proton to Kr (Fujimoto et al. 2004). We will discuss effects of neutrino interactions on heavy nuclei and uncertainty in nuclear reaction rates on nucleosynthetic results, in §4.2 and 4.3, respectively. While the abundances of ejecta from the outer region ( $r_{\text{ej,cc}} > 10,000 \text{ km}$ ) are set to be those before the core collapse (Rauscher et al. 2002). We note that the masses of the outer region, or  $r_{\text{ej,cc}} > 10,000 \text{ km}$ , is  $10.4 M_{\odot}$ . Moreover, when temperatures of the ejecta are greater than  $9 \times 10^9 \text{ K}$ , we set chemical composition of the ejecta to be that in nuclear statistical equilibrium (NSE), whose abundances are expressed with simple analytical expressions, specified by the density, temperature and electron fraction.

Electron fractions of the ejecta are re-evaluated during SN explosion coupled with the nuclear reaction network. The change in  $Y_e$  is taken into account through electron and positron captures on heavy nuclei, in addition to electron and positron captures on neutrons and protons as well as absorption of  $\nu_e$  and  $\bar{\nu}_e$  on neutrons and protons. The captures and absorptions on neutrons and protons are also taken into account in the hydrodynamic simulations. The rates for the captures and the absorptions are adopted from Fuller, Fowler, & Newman (1980, 1982) and Scheck et al. (2006), respectively.

It should be emphasized that post-processing electron fractions are slightly different (up to 10%) from those estimated with hydrodynamic simulations, in which the evolution of electron fractions is followed. This is because abundances of neutrons and protons in the network calculations are slightly different from those estimated with EOS in the hydrodynamic simulations. We note that 463 nuclei are taken into account in the network calculations, while only neutrons, protons,  $^4\text{He}$ , and a representative heavier nuclide are evaluated with EOS.

In the neutrino-heating dominated region, the abundances of neutrons and protons in the network calculations are larger than those evaluated with EOS. Hence, if we perform hydrodynamic simulations, in which abundances of nucleons are reliably evaluated with the reaction network, the neutrino heating rates in the simulations could increase compared to those in the current study, since the neutrino heating through the absorption of  $\nu_e$  and  $\bar{\nu}_e$  is dominant over the other heating reactions, and the heating rates via the absorption are proportional to the abundances of the nucleons.

The explosion energies also might increase. We emphasize that abundances of SN ejecta chiefly depends on the explosion energy and the mass of SN ejecta from an inner region, not on  $L_{\nu_e}$ , as shown in later.

### 3.2. Physical properties of SN ejecta

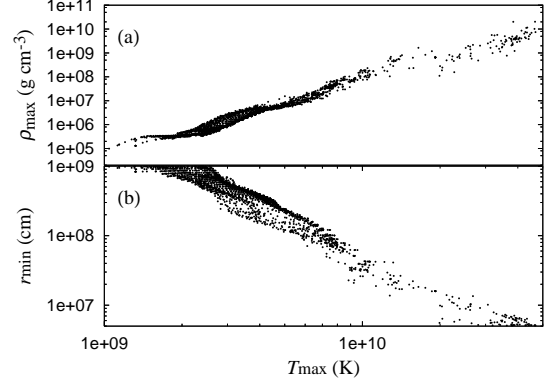


FIG. 3.— (a) Maximum densities vs. maximum temperatures of ejecta for model with  $L_{\nu_e} = 4.5 \times 10^{52} \text{ erg s}^{-1}$ . (b) Minimum radial position,  $r_{\text{min}}$  vs. maximum temperatures of ejecta for model with  $L_{\nu_e} = 4.5 \times 10^{52} \text{ erg s}^{-1}$ . Ejecta that falls near the proto neutron star have high densities  $> 10^9 \text{ g cm}^{-3}$  and temperatures  $> 10^{10} \text{ K}$ .

Maximum densities,  $\rho_{\text{max}}$ , and maximum temperatures,  $T_{\text{max}}$ , are good indicators for the composition of SN ejecta (Thielemann et al. 1996). Figure 3(a) shows  $\rho_{\text{max}}$  as a function of  $T_{\text{max}}$  of the ejecta for  $L_{\nu_e} = 4.5 \times 10^{52} \text{ erg s}^{-1}$ . Most of the ejecta with relatively low densities ( $< 10^8 \text{ g cm}^{-3}$ ) have  $\rho_{\text{max}}$  and  $T_{\text{max}}$  similar to those of ejecta in the spherical model of core collapse SNe (Thielemann et al. 1998). For some particles that have very high densities simultaneously with high temperatures ( $\rho_{\text{max}} \geq 10^9 \text{ g cm}^{-3}$  and  $T_{\text{max}} \geq 10^{10} \text{ K}$ ), electron captures operate to some extent, so that these particles become slightly neutron-rich,  $Y_e(10,000 \text{ km}) < 0.48$ . Here  $Y_e(10,000 \text{ km})$  represents the electron fraction for tracer particles evaluated when the particles reach  $r = 10,000 \text{ km}$ . This may be a useful quantity to measure  $Y_e$  of the ejecta, since  $Y_e$  closely freezes out at  $r > 10,000 \text{ km}$  (except for through  $\beta$ -decays at a later epoch). All ejecta with  $T_{\text{max}} > 10^{10} \text{ K}$  falls down to the heating region  $\leq 200\text{--}300 \text{ km}$  to be heated via neutrinos (Fig. 3(b)). For these neutrino-heated ejecta,  $\rho_{\text{max}}$  range from  $10^8\text{--}2 \times 10^{10} \text{ g cm}^{-3}$ .

For ejecta with higher  $\rho_{\text{max}}$ , electron captures on protons proceed more efficiently to make its  $Y_e$  smaller. Time evolution of physical quantities of such an ejecta is shown during the infall of the ejecta near the cooling region ( $r < 100 \text{ km}$ ) in Figure 4(a). As the density and temperature rise to more than  $10^9 \text{ g cm}^{-3}$  and  $10^{10} \text{ K}$ , respectively, the electron fraction decreases due to the electron captures. When the ejecta starts to be released via neutrino heating at  $t = 0.42 \text{ s}$ , the electron fraction increases through the absorption of  $\nu_e$  by neutrons. Finally  $Y_e(10,000 \text{ km})$  becomes 0.461 for the ejecta.

On the other hand, the electron captures on protons are not efficient for a proton-rich ejecta with  $Y_e(10,000 \text{ km}) = 0.559$ , as shown in Figure 4(b). This is because the densities of the inner region ( $r \leq 200 \text{ km}$ ) are relatively low ( $\leq 10^8 \text{ g cm}^{-3}$ ) due to the mass ejection during an earlier phase ( $\geq t_{\text{exp}}$ ). The electron fraction therefore remains constant and rises from 0.5 to 0.559 via the  $\nu_e$  absorption in an inner region  $r \leq 200 \text{ km}$ . The proton-richness in the ejecta is caused by the small energy

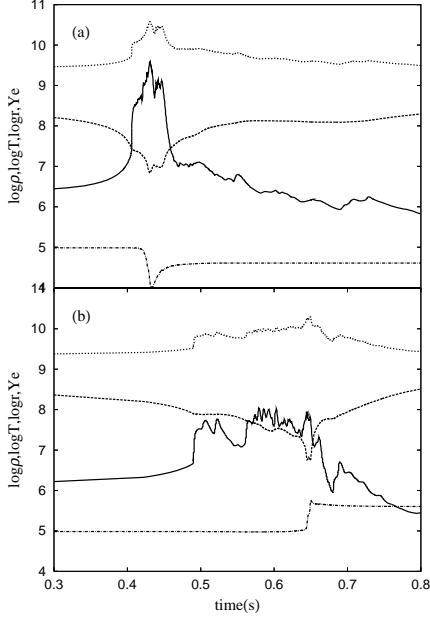


FIG. 4.— Time evolution of density, temperature, radial position, and electron fraction of an ejecta with (a)  $Y_e(10,000\text{km}) = 0.461$  and (b)  $Y_e(10,000\text{km}) = 0.559$ , for model with  $L_{\nu_e} = 4.5 \times 10^{52} \text{ erg s}^{-1}$ . Solid, dotted, dashed, and dash-dotted lines represent the density, temperature, radial position, and electron fraction of the ejecta, respectively. The electron fraction is shown with a value multiplied by ten. The density, temperature, and the radial position of the ejecta are presented in units of  $\text{g cm}^{-3}$ , K, and cm, respectively.  $Y_e$  of ejecta can largely change only in an inner region near the proto neutron star.

difference between  $\nu_e$  and  $\bar{\nu}_e$ . For  $T_{\nu_e}$  and  $T_{\bar{\nu}_e}$  adopted in our simulations, the relation,  $4(m_n - m_p) > \epsilon_{\bar{\nu}_e} - \epsilon_{\nu_e}$ , holds, which leads to  $Y_e > 0.5$  (Fröhlich et al. 2006a), where  $m_n$  and  $m_p$  are masses of neutron and protons, and  $\epsilon_{\bar{\nu}_e}$  and  $\epsilon_{\nu_e}$  are energies of anti-electron and electron neutrinos, respectively. We note that  $\epsilon_{\bar{\nu}_e} = 15.8 \text{ MeV}$  for  $T_{\bar{\nu}_e} = 5 \text{ MeV}$  and  $\epsilon_{\nu_e} = 12.6 \text{ MeV}$  for  $T_{\nu_e} = 4 \text{ MeV}$ .

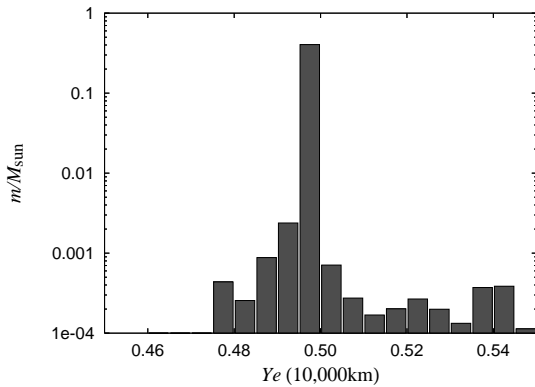


FIG. 5.— Masses as a function of  $Y_e(10,000\text{km})$  of ejecta from the inner region  $r_{\text{ej,cc}} \leq 10,000\text{km}$  for model with  $L_{\nu_e} = 4.5 \times 10^{52} \text{ erg s}^{-1}$ .

Figure 5 shows masses as a function of  $Y_e(10,000\text{km})$  of ejecta from the inner region  $r_{\text{ej,cc}} \leq 10,000\text{km}$ . We find that most of the ejecta (98.8%) have electron fractions of 0.49–0.5. Small fractions of the ejecta, 0.9% and 0.3% in mass, are slightly neutron-rich ( $0.46 < Y_e < 0.49$ ) and proton-rich ( $0.5 < Y_e < 0.56$ ), respectively. Masses of the slightly neutron- and proton-rich ejecta are larger for models with larger  $L_{\nu}$ , while the mass fractions of these ejecta are com-

parable for all the models.

### 3.3. Primary and secondary ejecta

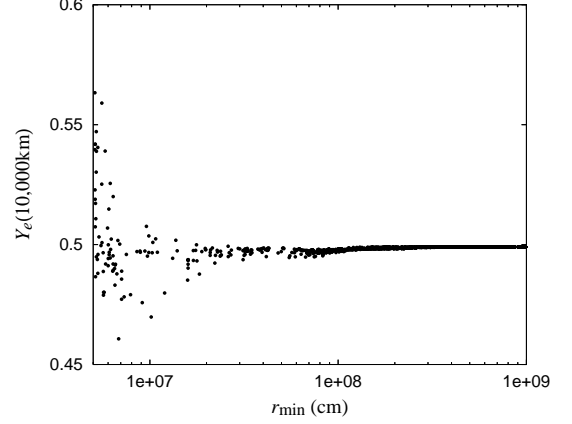


FIG. 6.—  $Y_e(10,000\text{km})$  vs. minimum radial position,  $r_{\text{min}}$ , of ejecta for model with  $L_{\nu_e} = 4.5 \times 10^{52} \text{ erg s}^{-1}$ .  $Y_e(10,000\text{km})$  are largely different from 0.5 only for ejecta that fall near the proto neutron star.

Electron fraction of an ejecta with the minimum radial position  $r_{\text{min}} \leq 200\text{--}300\text{km}$  changes due to high neutrino flux and/or efficient  $e^\pm$  capture (Fig. 4(a)). Figure 6 shows  $Y_e(10,000\text{km})$  as a function of  $r_{\text{min}}$  of the ejecta for model with  $L_{\nu_e} = 4.5 \times 10^{52} \text{ erg s}^{-1}$ . Hereafter, we refer to the ejecta with  $r_{\text{min}} \leq 200\text{km}$  as the *primary ejecta*, which have high maximum densities  $\geq 10^8 \text{ g cm}^{-3}$  and temperatures  $\geq 10^{10} \text{ K}$  (Fig. 3). The ejecta are heated through the neutrino heating. On the other hand, the others are referred as the *secondary ejecta*, heated chiefly via the shock wave driven by the primary ejecta.

It is true that  $Y_e$  of the primary ejecta could change if we adopt a more accurate neutrino-transfer scheme instead of the simplified light-bulb transfer scheme. Abundances of the primary ejecta are therefore highly uncertain because of the uncertainty on their  $Y_e$ . On the other hand, for the secondary ejecta,  $Y_e$  changes chiefly through the neutrino absorptions but the changes in  $Y_e$  are found to be less than 1% for almost all the secondary ejecta. In addition, for our typical 2D models that produce energetic explosions ( $L_{\nu_e} \geq 4.5 \times 10^{52} \text{ erg s}^{-1}$ ), the masses of the primary ejecta occupy only about 2% ( $8.7 \times 10^{-3} M_\odot$ ) in the ejecta from the inner region ( $0.41 M_\odot$  for  $r_{\text{ej,cc}} \leq 10,000\text{km}$ ). Therefore,  $Y_e$  of the secondary ejecta, whose mass is much larger than that of the primary ejecta, are unlikely to be largely changed even if we use a more accurate neutrino-transfer scheme. We conclude that masses of abundant nuclei, such as  $^{16}\text{O}$ ,  $^{28}\text{Si}$ , and  $^{56}\text{Ni}$ , do not largely change in the SN ejecta. We will discuss this point in §4.4.

The value of  $Y_e$  of the primary ejecta depends on the epoch of the ejection. The primary ejecta that eject in an early phase (before an epoch of 200–300 ms after the explosion ( $t_{\text{ej}} = 230\text{ms}$ )) are mainly neutron-rich, while the primary ejecta are proton-rich in the later phase. The proton-rich primary ejecta corresponds a kind of neutrino-driven winds, which are possibly not neutron-rich but proton-rich (Fischer et al. 2010; Hudepohl et al. 2010). Figure 7 shows  $Y_e(10,000\text{km})$  as a function of  $t(T_{\text{max}})$  of ejecta for model with  $L_{\nu_e} = 4.5 \times 10^{52} \text{ erg s}^{-1}$ , where  $t(T_{\text{max}})$  is defined as the time when the temperature of ejecta attains to their maximum value,  $T_{\text{max}}$ . We note that the gas starts to be ejected just after  $t = t(T_{\text{max}})$ , as shown in Figure 4. We note that the dependence of  $Y_e$  on the

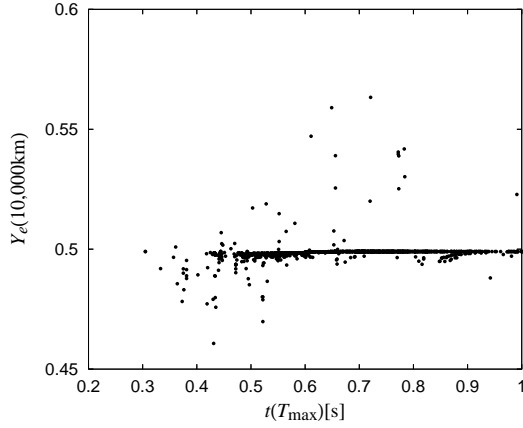


FIG. 7.—  $Y_e$  vs.  $t(T_{\max})$ , the time when the temperature of ejecta attains to  $T_{\max}$  for model with  $L_{\nu_e} = 4.5 \times 10^{52} \text{ erg s}^{-1}$ . Ejecta at an early phase ( $< 200$ – $300$  ms after the explosion) tend to be neutron-rich, while proton-rich in the later phase.

epoch of the ejection also appears in a spherical simulation of SN explosion of a star with an ONeMg core using an elaborated code taking into account an accurate neutrino transfer scheme (Kitaura et al. 2006; Wanajo et al. 2009).

### 3.4. Masses and abundances of ejecta

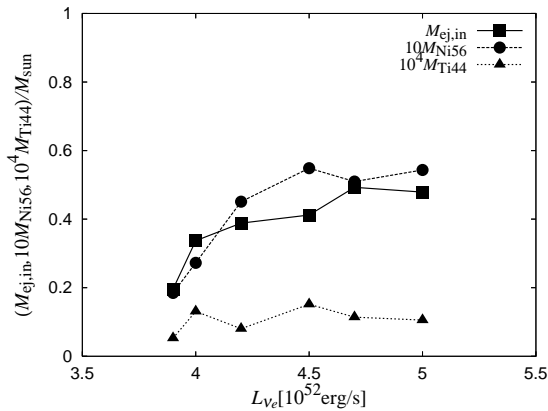


FIG. 8.— Mass of the ejecta from the inner region and masses of radioactives vs.  $L_{\nu_e}$ . Note in a spherical model by Rauscher et al. (2002) that the obtained masses of  $^{56}\text{Ni}$  and  $^{44}\text{Ti}$  are  $0.11M_{\odot}$  and  $1.4 \times 10^{-5}M_{\odot}$ , respectively.

Masses of nuclei, such as  $^{56}\text{Ni}$ ,  $^{57}\text{Ni}$ ,  $^{58}\text{Ni}$  and  $^{44}\text{Ti}$ , have been estimated in some SN remnants; For SN1987A, masses of  $^{56}\text{Ni}$  and  $^{44}\text{Ti}$  are deduced to be  $\simeq 0.07M_{\odot}$  (Shigeyama et al. 1988; Woosley 1988) and  $1 - 2 \times 10^{-4}M_{\odot}$  (Nagataki 2000, and references therein), respectively. The estimated mass of  $^{44}\text{Ti}$  is comparable to that in Cas A ( $1.6^{+0.6}_{-0.3} \times 10^{-4}M_{\odot}$ ) (Renaud et al. 2006) and greater than that in the youngest Galactic supernova remnant G1.9+0.3 ( $1 - 7 \times 10^{-5}M_{\odot}$ ) (Borkowski et al. 2010), which may originate from a Type Ia event. Figure 8 shows masses of SN ejecta ejected from the inner region ( $r_{\text{ej.cc}} \leq 10,000 \text{ km}$ ),  $M_{\text{ej.in}}$ , and masses of  $^{56}\text{Ni}$  and  $^{44}\text{Ti}$ . Masses of the ejecta from the inner region of  $r_{\text{ej.cc}} \leq 10,000 \text{ km}$  (solid line with filled squares) and masses of  $^{56}\text{Ni}$  (dashed line with filled circles) and  $^{44}\text{Ti}$  (dotted line with filled triangles) are shown with a value times a factor of 1, 10 and  $10^4$ , respectively. We find that masses of the ejecta and  $^{56}\text{Ni}$  roughly correlate with the neutrino lumi-

nosities. The masses of  $^{56}\text{Ni}$  and  $^{44}\text{Ti}$  are less than and comparable to those in the spherical model (Rauscher et al. 2002), or  $0.11M_{\odot}$  and  $1.4 \times 10^{-5}M_{\odot}$ , respectively. Note that the explosion energy is  $1.2 \times 10^{51} \text{ erg}$  in the model. We find that  $^{44}\text{Ti}$  relative to  $^{56}\text{Ni}$  are much smaller than those in the solar system, in SN1987A, and in Cas A, but comparable to that in the supernova remnant G1.9+0.3.  $^{57}\text{Ni}$  relative to  $^{56}\text{Ni}$  is comparable to those in the solar system and in SN1987A, while  $^{58}\text{Ni}$  relative to  $^{56}\text{Ni}$  is overproduced compared with those in the solar system and in SN1987A, because they are abundantly produced in the slightly neutron-rich ejecta (Hashimoto 1995; Nagataki et al. 1997).

It should be emphasized that  $^{44}\text{Ti}$  is underproduced in our simulations of the SN explosion, contrary to the overproduction in the previous 2D results (Nagataki et al. 1997), in which the explosion energy is aspherically and artificially added and the remnant mass is set to a value in order that the ejected mass of  $^{56}\text{Ni}$  is reproduced the mass observed in SN1987A in Nagataki et al. (1997). The underproduction is possibly caused by a larger remnant mass in our models. This is because the explosion energy and the ratio of the explosion energy on the polar axis to that on the equatorial plane are comparable to those evaluated in our simulation, and masses of  $^{44}\text{Ti}$  as well as  $^{56}\text{Ni}$  have shown to strongly depend on the value of the remnant mass in 2D calculations (Young et al. 2006).

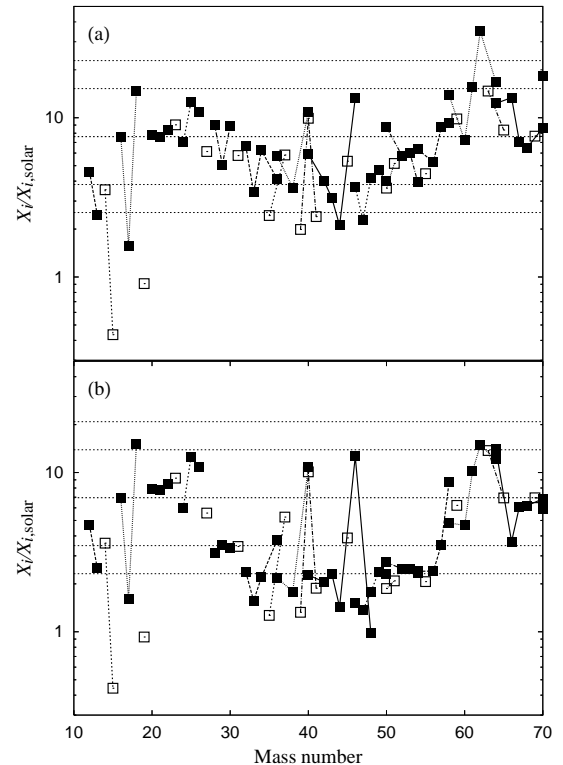


FIG. 9.— Overproduction factors,  $X_i/X_{\text{O},i}$  vs. mass number for (a)  $L_{\nu_e} = 4.5 \times 10^{52} \text{ erg s}^{-1}$  and for (b)  $L_{\nu_e} = 3.9 \times 10^{52} \text{ erg s}^{-1}$ . Thick horizontal-dashed lines represents a factor equals to that of  $^{16}\text{O}$ , while two normal and two thin lines denote a factor equals to that of  $^{16}\text{O}$  times 2, 1/2, 3, and 1/3, respectively.

In order to compare estimated abundances with the solar system ones (Anders & Grevesse 1989), we have integrated masses of nuclei over all the ejecta to evaluate the abundances of the SN ejecta. Figure 9(a) shows overproduction



factors after decays as a function of the mass number,  $A$  for  $L_{\nu_e} = 4.5 \times 10^{52} \text{ erg s}^{-1}$ , in which the explosion energy is  $1.3 \times 10^{51} \text{ erg s}^{-1}$  (Fig. 2(a)) and  $M_{\text{ej, in}}$  is  $0.41 M_{\odot}$  (Fig. 8). We find that the abundance pattern of the SN ejecta is similar to the solar system one. We note that  $^{17}\text{O}$ , which is underproduced in the ejecta, can be abundantly synthesized in Type Ia SNe, and that  $^{15}\text{N}$  and  $^{19}\text{F}$  are comparably produced if neutrino effects are taken into account (Woosley & Weaver 1995), as shown later in Figure 14. We point out that  $^{64}\text{Zn}$ , which is underproduced in the spherical case (Rauscher et al. 2002), is abundantly produced in slightly neutron-rich ejecta ( $0.46 \leq Y_e \leq 0.49$ ).

In the ejecta, however, the neutron-rich Ni,  $^{62}\text{Ni}$ , is overproduced. The overproduction of the neutron-rich Ni isotopes has also appeared in the spherical models (Hashimoto 1995; Rauscher et al. 2002) as well as in the asymmetric model (Nagataki et al. 1997). The overproduction has been suppressed if the electron fraction of slightly neutron-rich material ( $Y_e = 0.495$  just before the core collapse) near the mass cut is artificially modified to 0.499 (Hashimoto 1995; Nagataki et al. 1997). Hence, it has been remarked that the overabundance of the neutron-rich Ni isotopes may inherit the uncertainty in the progenitor model, in particular in the neutronization due to the combined effects of convective mixing, electron captures, and positron decays during their Si burning stage (Hashimoto 1995). In our aspherical models, the overabundances of Ni in the primary neutron-rich ejecta are not large, other than  $^{60}\text{Ni}$ , as we will discuss later (§4.4). The overproduction of Ni mainly takes place in slightly neutron-rich secondary ejecta ( $0.49 < Y_e < 0.5$ ). We find that the electron fractions of the secondary ejecta are 0.4985 just before the core collapse and decrease by up to 1% through the neutrino absorptions. Therefore, the overabundance of  $^{62}\text{Ni}$  possibly inherits the uncertainty not only in the progenitor model but also in the change for  $Y_e$  during the SN explosion. Moreover, the overproduction of Ni isotopes are also shown to be reduced in the ejecta from the spherical SN explosion induced via artificially enhanced neutrino heating (Fröhlich et al. 2006a).

On the other hand, the integrated abundances are largely different from those in the solar system for  $L_{\nu_e} = 3.9 \times 10^{52} \text{ erg s}^{-1}$ , in which  $E_{\text{exp}} = 0.45 \times 10^{51} \text{ erg s}^{-1}$  and  $M_{\text{ej, in}} = 0.20 M_{\odot}$ . Nuclei with  $A \geq 28$  are deficient in the model (Fig. 9(b)), compared with O, which is mainly ejected from outer layers. The overproduction factors of nuclei lighter than  $^{27}\text{Al}$  are very similar for both models, because these nuclei are mainly synthesized during the hydrostatic burning. While nuclei heavier than Si are mainly produced during the SN explosion through the explosive burning in ejecta from the inner region ( $r_{\text{ej, cc}} \leq 10,000 \text{ km}$ ).

The abundance patterns for models with  $M_{\text{ej, in}} \sim (0.4 - 0.5) M_{\odot}$ , or those with  $L_{\nu_e} = (4.5, 4.7, \text{ and } 5.0) \times 10^{52} \text{ erg s}^{-1}$ , are similar to that in the solar system. We should notice that  $M_{\text{ej, in}}$ , which corresponds to masses of a neutron star, estimated as  $(1.54 - 1.62) M_{\odot}$  for these models (Fig. 2(b)), are comparable to the baryonic mass (around  $1.5 M_{\odot}$ ) of a neutron star for observed neutron-star binaries, in which the progenitor of the neutron star seems to be a star with a Fe core (Schwab et al. 2010). Moreover,  $E_{\text{exp}}/M_{\text{ej}} = (0.92 - 1.2) \times 10^{50} \text{ erg}/M_{\odot}$  evaluated for the models are comparable to the value  $E_{\text{exp}}/M_{\text{ej}} = 0.76 \times 10^{50} \text{ erg}/M_{\odot}$  estimated in SN 1987A (Shigeyama & Nomoto 1990). The time from the core collapse to the explosion,  $t_{\text{exp}}$ , is  $\sim 0.2 \text{ s}$  (Fig. 2(b)), which is

enough to grow a low-mode SASI. The growth is appropriate for explaining the distributions and velocities of nuclei observed in SN 1987A, as shown in Kifonidis et al. (2006).

### 3.5. Aspherical infall

The value of  $M_{\text{ej, in}}$  depends on  $E_{\text{exp}}$  as well as aspherical matter infall to the neutron star, while the masses of  $^{56}\text{Ni}$  correlates with  $E_{\text{exp}}$  (Figs. 2(a) and 8). Figure 10 shows the position of SN ejecta before the core collapse for model with  $L_{\nu_e} = 4.5 \times 10^{52} \text{ erg s}^{-1}$ . Filled squares, filled circles, filled triangles, and open triangles indicate ejecta, which correspond to the complete Si burning ( $T_{\text{max, 9}} \geq 5$  where  $T_{\text{max, 9}} = T_{\text{max}}/10^9 \text{ K}$ ), the incomplete Si burning ( $4 \leq T_{\text{max, 9}} \leq 5$ ), the O burning ( $3.3 \leq T_{\text{max, 9}} \leq 4$ ), and the C/Ne burning ( $1 \leq T_{\text{max, 9}} \leq 3.3$ ), respectively. We find that whole of the iron core ( $\sim 2,000 \text{ km}$ ) collapses to the proto neutron star and that the infall of material to the proto neutron star is aspherical; Larger amounts of the gas infall from the upper hemisphere compared with from the lower half. Larger amounts of material aspherically infall to the neutron star for model with  $L_{\nu_e} = 4.5 \times 10^{52} \text{ erg s}^{-1}$  compared with model with  $L_{\nu_e} = 5.0 \times 10^{52} \text{ erg s}^{-1}$ . Though  $E_{\text{exp}}$  is comparable,  $M_{\text{ej, in}}$  for  $L_{\nu_e} = 4.5 \times 10^{52} \text{ erg s}^{-1}$  is smaller than that for  $L_{\nu_e} = 5.0 \times 10^{52} \text{ erg s}^{-1}$ .

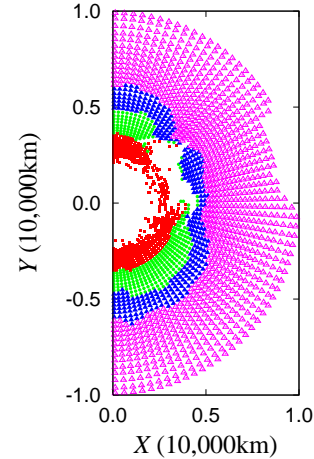


FIG. 10.— Initial position of SN ejecta that are released from the inner region ( $r_{\text{cc}} < 10,000 \text{ km}$ ) for model with  $L_{\nu_e} = 4.5 \times 10^{52} \text{ erg s}^{-1}$ .

### 3.6. Aspherical distribution of energy and nuclei

Distributions of the energy and abundances of SN ejecta are highly aspherical, as one can expect from the entropy distribution (Fig. 1). The distributions are shown for  $L_{\nu_e} = 4.5 \times 10^{52} \text{ erg s}^{-1}$  at  $t = 1.5 \text{ s}$  in Figure 11. The energy and abundances are presented in units of  $10^{47} \text{ erg}$  and normalized by the solar abundances, respectively, for logarithm scale. It should be emphasized that the distributions change during later expansion phase (Kifonidis et al. 2006; Gawryszczak et al. 2010). We note that the secondary ejecta that is located in outer layers ( $r_{\text{ej, cc}} > 10,000 \text{ km}$ ) are not shown in the figures. The high energy ejecta concentrates on the shock front, in particular in polar regions ( $\theta < \pi/4, \theta > 3\pi/4$ ). Both Si and O burning proceed to produce  $^{56}\text{Ni}$  and  $^{28}\text{Si}$  abundantly in the region. We emphasize that a deformed shell structure forms with Fe, Si and O layers from inside to outside in the secondary ejecta heated via the shock wave. Composition of the secondary ejecta depends chiefly on  $T_{\text{max}}$ , which

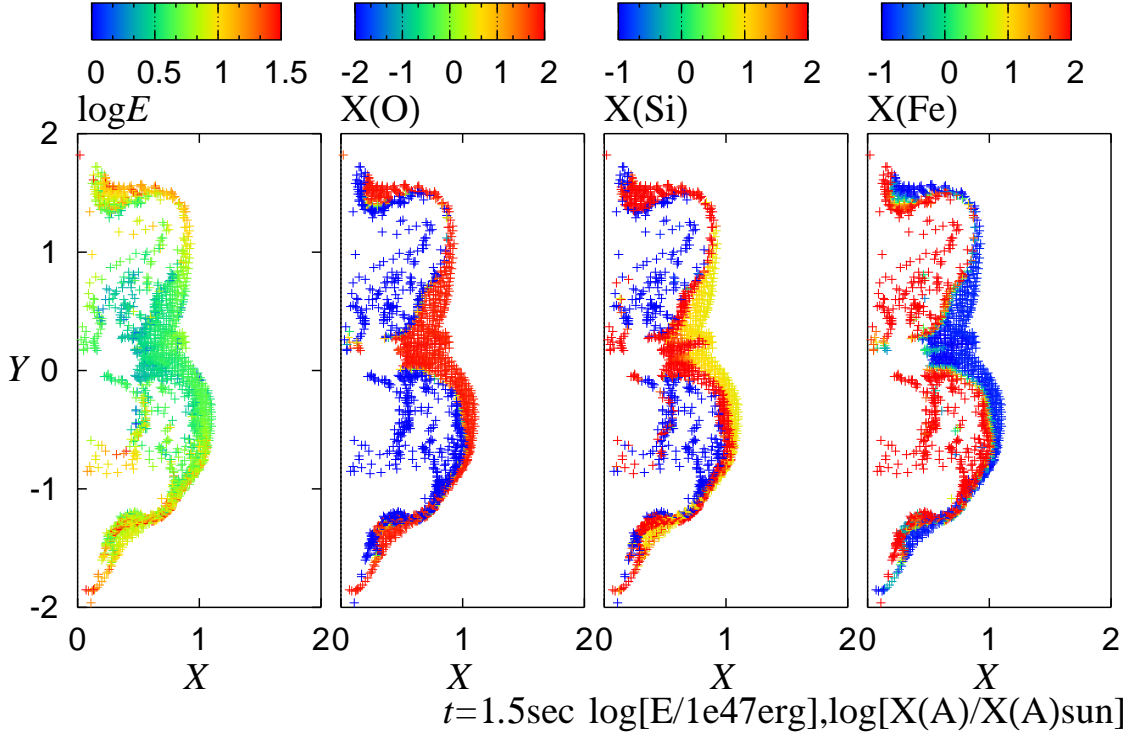


FIG. 11.— Distribution of the energy and abundances of the ejecta for  $L_{\nu_e} = 4.5 \times 10^{52} \text{ erg s}^{-1}$  at  $t = 1.5 \text{ s}$  in a region of  $0 \leq x \leq 20,000 \text{ km}$  and  $-20,000 \text{ km} \leq y \leq 20,000 \text{ km}$ . Abundances are shown in units of those in the solar system for  $^{16}\text{O}$ ,  $^{28}\text{Si}$ , and Fe, which is the sum of  $^{56}\text{Fe}$ ,  $^{56}\text{Ni}$ , and  $^{54}\text{Fe}$ .

is determined via the shock heating. The shell structure is therefore formed in the secondary ejecta, because  $T_{\text{max}}$  gradually decreases from inner to outer layers, where the structure is highly aspherical and deformed. We note that Ca is co-produced with  $^{28}\text{Si}$ , as in the spherical models.

The primary ejecta however do not form such a structure. This is because physical properties of the ejecta, which are mainly heated via neutrinos to be  $> 10^{10} \text{ K}$  (Fig. 4), are independent from their positions, and thus their compositions are also independent. A fraction of the primary ejecta that are mainly composed of Fe and Ni is found to be mixed into the deformed layers, while a small amount of the secondary ejecta falls towards the neutron star through near the equatorial plane. Consequently, the ejecta with abundant O and/or Si appear in the central region ( $r < 2,000 \text{ km}$ ). Due to such mixings and infall, some of the Si- and O-rich ejecta can penetrate deeper into the Fe-rich ejecta, which is in sharp contrast to spherical models.

We have averaged energy and masses of nuclei of the inner ejecta over a radial direction. We note that the energy and masses of the outer ejecta ( $r_{\text{ej,cc}} > 10,000 \text{ km}$ ) are not included in an averaging procedure. If we include ejecta from the outer layers, the asymmetry of  $^{16}\text{O}$  becomes small, because of the existence of spherically distributed  $^{16}\text{O}$  in the layers. Figure 12(a) shows the averaged energy and masses of  $^{16}\text{O}$ ,  $^{28}\text{Si}$ , and  $^{56}\text{Ni}$ . Asphericity of the energy is prominent; Ratio of the energy at  $\theta = \pi/2$  to that at  $\theta = 0$  is  $\sim 4$  and ratio of the maximum to the minimum energy is  $\sim 8$ . We note that the ratios are comparable to those in two-dimension models (Nagataki et al. 1997, models A2 and A3). Only a small amount of  $^{56}\text{Ni}$  exists near the equatorial plane ( $\theta \sim (0.8 - 1.6) \text{ rad.}$ ), where the energy is lower compared with that near the polar axis. The asymmetry of  $^{28}\text{Si}$  mass is similar to that of the energy and smaller than that of  $^{56}\text{Ni}$ . Mass distribution of  $^{44}\text{Ti}$  is very similar to that of  $^{56}\text{Ni}$ , as in spherical mod-

els, because both nuclei are produced in the secondary ejecta through  $\alpha$ -rich freezeout. The peaks of  $^{28}\text{Si}$  mass around the polar directions are misaligned with those of  $^{56}\text{Ni}$  around  $\theta \sim \pi/4$  and  $3\pi/4$ , although the misalignment could disappear due to the lateral motion of the ejecta, during later explosion phase ( $\leq 300 \text{ s}$ ) as pointed out in Gawryszczak et al. (2010). We note that the lateral motion does not follow during the later phase in the present study.

In addition to the mass fractions of nuclei, number ratios of nuclei relative to O ( $^{16}\text{O}$ ) are important quantities, because the ratios are indicative to the production and destruction mechanism of nuclei. Angular distributions of the number ratio are shown for the inner ejecta ( $r_{\text{ej,cc}} \leq 10,000 \text{ km}$ ) averaged over a radial direction for  $L_{\nu_e} = 4.5 \times 10^{52} \text{ erg s}^{-1}$  in Figure 12(b). Ratio of Ne ( $^{20}\text{Ne}$ , solid line) is 0.1-0.2 for a direction where the O/Ne burning does not effectively operate, while it becomes much lower in a region where the O/Ne burning effectively operates to synthesize abundant Si and/or Fe relative to O. Distribution of the number ratio  $N(\text{Mg})/N(\text{O})$  ( $^{24}\text{Mg}$ , dash-dotted line) is similar to the spherical case, because Mg is produced during both the stellar evolution and the explosion through the same process, or the O/Ne burning, with which  $N(\text{Mg})/N(\text{O})$  becomes  $\sim 0.05$  for a  $15M_{\odot}$  progenitor. Here  $N(X)$  is the number of nuclei, X. Ratio of Si ( $^{28}\text{Si}$ , dashed line) anti-correlates with that of Fe (the sum of  $^{56}\text{Ni}$ ,  $^{56}\text{Fe}$ , and  $^{54}\text{Fe}$ , dotted line). This is because Fe is produced via the burning of Si.

## 4. DISCUSSIONS

### 4.1. Dependences on neutrino temperatures

We have assumed the neutrino spheres with given luminosities and with the Fermi-Dirac distribution of neutrino temperatures, and considered models with neutrino temperatures,  $T_{\nu_e}$ ,  $T_{\bar{\nu}_e}$ , and  $T_{\nu_x}$  as 4 MeV and 5 MeV, and 10 MeV,



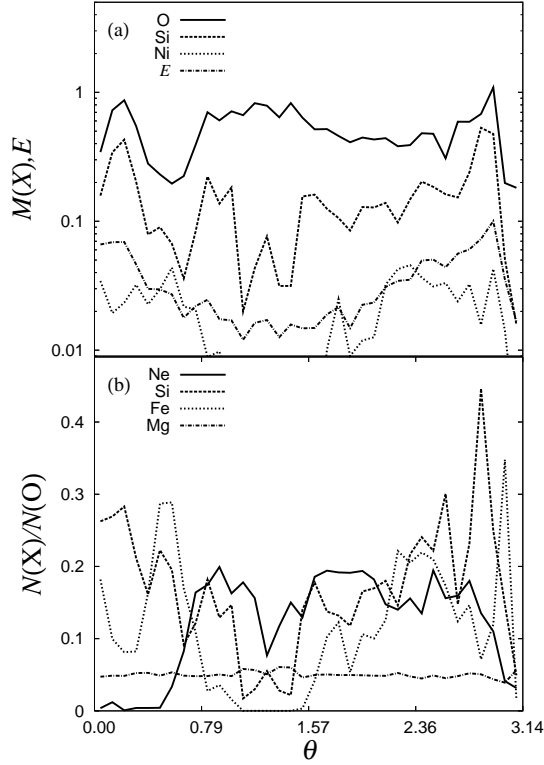


FIG. 12.— (a) Angular distribution of the averaged energy and masses of nuclei of the inner ejecta ( $r_{\text{ej,cc}} \leq 10,000 \text{ km}$ ) over a radial direction for  $L_{\nu_e} = 4.5 \times 10^{52} \text{ erg s}^{-1}$  at  $t = 1.5 \text{ s}$ . Solid, dashed, dotted, and dash-dotted lines indicate the averaged mass of  $^{16}\text{O}$ ,  $^{28}\text{Si}$ , and  $^{56}\text{Ni}$  and the averaged energy, respectively. The masses and energy are shown in units of  $0.01 M_\odot$  and  $10^{51} \text{ erg}$ , respectively. (b) Angular distribution of number ratios of nuclei to  $^{16}\text{O}$  of the inner ejecta ( $r_{\text{ej,cc}} \leq 10,000 \text{ km}$ ) averaged over a radial direction for  $L_{\nu_e} = 4.5 \times 10^{52} \text{ erg s}^{-1}$  at  $t = 1.5 \text{ s}$ . Solid, dashed, dotted, and dash-dotted lines indicate the ratios of  $^{20}\text{Ne}$ ,  $^{28}\text{Si}$ , iron, and  $^{24}\text{Mg}$ , respectively. The iron consists from  $^{56}\text{Ni}$ ,  $^{56}\text{Fe}$ , and  $^{54}\text{Fe}$ .

TABLE 1  
MODEL PARAMETERS AND PROPERTIES OF THE EXPLOSION FOR NINE EXPLODED MODELS

$T_{\nu_e}$	$T_{\bar{\nu}_e}$	$L_{\nu_e}$	$E_{\text{exp}}$	$t_{\text{exp}}$	$M_{\text{pNS}}$	$M_{\text{ej,in}}$	$M(^{56}\text{Ni})$	$M(^{44}\text{Ti})$
4.0	5.0	3.9	0.45	1.20	1.84	0.20	1.85e-2	5.29e-6
4.0	5.0	4.0	0.80	0.31	1.70	0.34	2.72e-2	1.31e-5
4.0	5.0	4.2	1.02	0.31	1.65	0.39	4.51e-2	8.04e-6
4.0	5.0	4.5	1.30	0.23	1.62	0.41	5.49e-2	1.52e-5
4.0	5.0	4.7	1.03	0.21	1.54	0.49	5.10e-2	1.14e-5
4.0	5.0	5.0	1.30	0.18	1.56	0.48	5.44e-2	1.05e-5
3.6	4.5	4.0	0.35	1.41	1.93	0.11	1.10e-2	6.95e-6
3.6	4.5	4.5	0.35	1.19	1.87	0.17	1.40e-2	5.53e-6
3.6	4.5	5.0	0.45	0.62	1.83	0.21	1.73e-2	6.38e-6

NOTE. — Each column shows  $T_{\nu_e}$ ,  $T_{\bar{\nu}_e}$ ,  $L_{\nu_e}$ ,  $E_{\text{exp}}$ ,  $t_{\text{exp}}$  and masses ( $M_{\text{pNS}}$ ,  $M_{\text{ej,in}}$ ,  $M(^{56}\text{Ni})$ , and  $M(^{44}\text{Ti})$ ), in units of MeV, MeV,  $10^{52} \text{ erg s}^{-1}$ ,  $10^{51} \text{ erg}$ , s, and  $M_\odot$ , respectively.

respectively. The temperatures are however slightly lower and change in time, as shown in simulations using a more elaborate numerical code (Marek et al. 2009; Marek & Janka 2009). In order to evaluate dependences of hydrodynamic and nucleosynthetic results on neutrino temperatures, we have performed simulations for three models with lower neutrino temperatures;  $T_{\nu_e} = 3.6 \text{ MeV}$ ,  $T_{\bar{\nu}_e} = 4.5 \text{ MeV}$ , and  $T_{\nu_x} = 9 \text{ MeV}$ , and  $L_{\nu_e} = (4.0, 4.5, \text{ and } 5.0) \times 10^{52} \text{ erg s}^{-1}$ . We find that, for a given  $L_{\nu_e}$ , the explosions are much weaker for a lower  $T_{\nu_e}$

model, in spite of only 10% changes in neutrino temperatures. Table 1 summarizes hydrodynamic and nucleosynthetic properties for the nine models that produce explosions, in which  $T_{\nu_e}$ s are changed in the three ways as mentioned above. The explosion energies are  $(0.35, 0.35, \text{ and } 0.45) \times 10^{51} \text{ erg}$  for models with  $L_{\nu_e} = (4.0, 4.5, \text{ and } 5.0) \times 10^{52} \text{ erg s}^{-1}$ , respectively. Mass of the ejecta from the inner region ( $r_{\text{ej,cc}} \leq 10,000 \text{ km}$ ),  $M_{\text{ej,in}}$ , and  $^{56}\text{Ni}$  mass are  $0.11 - 0.21 M_\odot$  and  $0.011 - 0.017 M_\odot$ , respectively. Figure 13 shows overproduction factors for the low  $T_{\nu_e}$  model with  $L_{\nu_e} = 5.0 \times 10^{52} \text{ erg s}^{-1}$ . We emphasize that the overproduction factors are very similar to those for the high  $T_{\nu_e}$  model with  $L_{\nu_e} = 3.9 \times 10^{52} \text{ erg s}^{-1}$ , in which the explosion energy and the ejecta mass from the inner region are comparable to the above model, or  $0.45 \times 10^{51} \text{ erg}$  and  $0.020 M_\odot$ , respectively. We conclude that the abundances of the ejecta do not directly depend on  $T_{\nu_e}$  but mainly depend on the explosion energy and the ejecta mass.

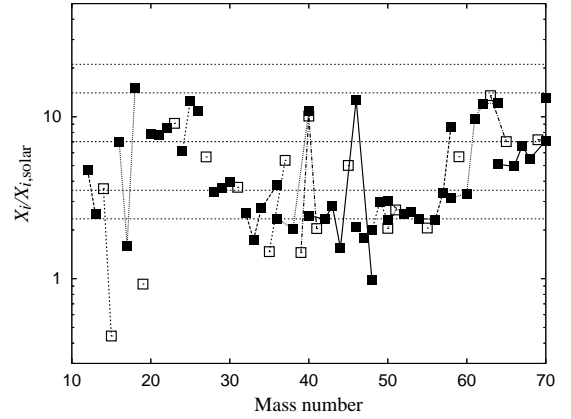


FIG. 13.— Same as Figure 9 but for model with low neutrino temperatures and  $L_{\nu_e} = 5.0 \times 10^{52} \text{ erg s}^{-1}$ . The factors are very similar to those for a model with high neutrino temperatures and  $L_{\nu_e} = 3.9 \times 10^{52} \text{ erg s}^{-1}$ , as shown in Figure 9(b).

#### 4.2. Effects of the $\nu$ interactions on heavy nuclei

Effects of neutrino interactions on SN ejecta have been investigated for spherical SN explosion (Woosley et al. 1990; Woosley & Weaver 1995). We have calculated abundances of the ejecta taking into account  $\nu$  interactions on heavy nuclei (Goriely et al. 2001) for  $L_{\nu_e} = 4.5 \times 10^{52} \text{ erg s}^{-1}$ . Cross sections for the neutrino reactions are taken from Woosley et al. (1990), in which rates are included for neutral and charged current reactions on He and from C to Kr. Figure 14 shows ratios of the abundances of the ejecta with the  $\nu$  interactions to those without the interactions. We find that the increase of the abundances due to the interactions of  $\nu$  on heavy nuclei are up to 50%, except for  $^{19}\text{F}$ , whose ratio is 2.1.  $^{19}\text{F}$  is enhanced via the neutral and charged current interactions of  $^{20}\text{Ne}$ , or  $^{20}\text{Ne}(\nu\nu', p)^{19}\text{F}$  and  $^{20}\text{Ne}(\bar{\nu}_e, e^+n)^{19}\text{F}$ , respectively.  $^{15}\text{N}$  and  $^{50}\text{V}$  are synthesized through  $^{16}\text{O}(\nu\nu', p)^{15}\text{N}$  and  $^{50}\text{Cr}(\bar{\nu}_e, e^+)^{50}\text{V}$ , respectively. We note that the enhancement of light elements, such as Li, Be, and B, via the  $\nu$  interactions is not fully taken into account in our calculation, because the composition of ejecta from outer layers ( $r_{\text{ej,cc}} > 10,000 \text{ km}$ ) is fixed to be the pre-SN composition, although the production of these elements is efficient in the outer layers through neutrino interactions (Woosley et al. 1990; Yoshida et al. 2008). Moreover, neutrino absorptions

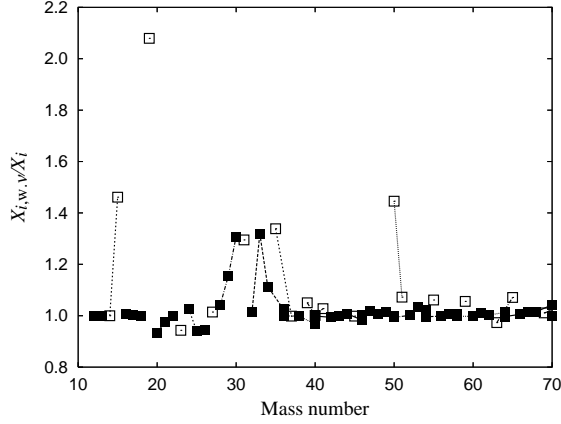


FIG. 14.— Ratios of the abundances of SN ejecta taking into account  $\nu$  interactions on heavy nuclei to those without the  $\nu$  interactions, as a function of  $A$  for  $L_{\nu_e} = 4.5 \times 10^{52} \text{ erg s}^{-1}$ .

on D may be important for nucleosynthesis as well as the dynamics of the SN explosion (Nakamura et al. 2009).

#### 4.3. Dependences of abundances on nuclear reaction rates

We have adopted reaction rates mainly taken from the REACLIB database in our nuclear reaction network presented in §3.1. The database is recently updated and continuously maintained by the Joint Institute for Nuclear Astrophysics (JINA) REACLIB project (Cyburt et al. 2010). We have calculated abundances of the ejecta for  $L_{\nu_e} = 4.5 \times 10^{52} \text{ erg s}^{-1}$  adopting reaction rates taken from the JINA REACLIB V1.0 database. Figure 15 shows ratios of the abundances of the ejecta adopting reaction rates in the JINA REACLIB V1.0 database to those in REACLIB database. We find that the differences are small, up to 30%, between abundances with the JINA REACLIB V1.0 and REACLIB databases. If we use newly evaluated  $\alpha$ -capture rates on  $^{40}\text{Ca}$  and  $^{44}\text{Ti}$ , yields of  $^{44}\text{Ti}$  are likely to be lower (Hoffman et al. 2010).

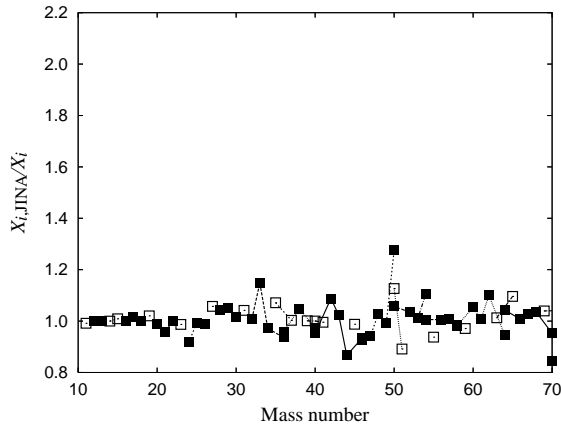


FIG. 15.— Ratios of the abundances of SN ejecta using reaction rates in the JINA REACLIB V1.0 database to those in REACLIB database, as a function of  $A$  for  $L_{\nu_e} = 4.5 \times 10^{52} \text{ erg s}^{-1}$ .

#### 4.4. Uncertainty of abundances of the ejecta

As shown in §3.3, the ejecta consists of the primary ejecta, whose  $Y_e$  and thus abundances are highly uncertain and the secondary ejecta, which have a relatively definite composition and are much heavier than the primary ejecta. In order to clarify uncertainty on the estimate of abundances of

the ejecta, we have evaluated abundances of the ejecta being integrated over ejecta without the primary ejecta and have compared above the abundances with those summed over all the ejecta (Fig. 9(a)). Figure 16 shows ratios of the abundances of all the ejecta to those without the primary ejecta for  $L_{\nu_e} = 4.5 \times 10^{52} \text{ erg s}^{-1}$ . We find that abundances of most of nuclei with  $A \leq 70$  do not largely change within a factor of 2. The overproduction factors are therefore very similar to those in Figure 9(a). The ratios are greater than 1.5 for  $^{43}\text{Ca}$ ,  $^{45}\text{Sc}$ ,  $^{47}\text{Ti}$ ,  $^{50}\text{Ti}$ ,  $^{54}\text{Cr}$ ,  $^{60}\text{Ni}$ ,  $^{64}\text{Zn}$ ,  $^{66}\text{Zn}$ , and  $^{70}\text{Ge}$ , in particular, 9.0, 2.8, and 3.1 for  $^{64}\text{Zn}$ ,  $^{66}\text{Zn}$ , and  $^{70}\text{Ge}$ , respectively. These nuclei are therefore chiefly synthesized in the primary ejecta, not in the secondary ejecta. Moreover,  $^{50}\text{Ti}$ ,

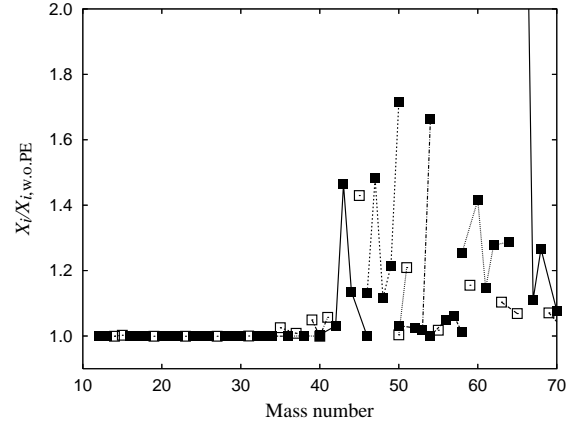


FIG. 16.— Ratios of the abundances of SN ejecta to those without the primary ejecta, as a function of  $A$  for  $L_{\nu_e} = 4.5 \times 10^{52} \text{ erg s}^{-1}$ .

$^{54}\text{Cr}$ ,  $^{60}\text{Ni}$ ,  $^{64}\text{Zn}$ ,  $^{66}\text{Zn}$ , and  $^{70}\text{Ge}$  are synthesized in neutron-rich primary ejecta, while  $^{43}\text{Ca}$ ,  $^{45}\text{Sc}$ ,  $^{47}\text{Ti}$ , and  $^{60}\text{Ni}$  are abundantly produced in proton-rich primary ejecta through  $\nu p$ -processes (Fröhlich et al. 2006a,b; Pruet et al. 2006; Wanajo 2006).

In short, abundances of  $^{64}\text{Zn}$ ,  $^{66}\text{Zn}$ , and  $^{70}\text{Ge}$  are highly uncertain but those of the other nuclei are relatively definite. If a fraction of the primary ejecta could become much larger, abundances might be highly uncertain, in particular for the nuclei that are produced in the primary ejecta. The fraction is however unlikely to be much larger, because the ejection of the secondary ejecta is driven by the shock wave caused by the primary ejecta. It should be noted that the mass fractions of the primary ejecta to the secondary ejecta are comparable for all the models, although the explosion energies and ejected masses from the inner region diverse among the models.

Moreover, matter near the proto neutron star is blown off via neutrino-driven winds during later evolution of the star ( $> 2 \text{ s}$ ). The ejecta could be not neutron-rich but proton-rich ( $Y_e \sim 0.5 - 0.6$ ) and have high entropy ( $> 50 k_B$ ) (Fischer et al. 2010; Hüpdepohl et al. 2010). The  $\nu p$ -process could operate in the ejecta to synthesize light p-nuclei (Fröhlich et al. 2006a,b; Pruet et al. 2006; Wanajo 2006). However, the process may have not large contributions to the ejected masses of abundant nuclei, since the mass ejection rate is small through the winds at the later epoch (Hüpdepohl et al. 2010).

#### 4.5. Comparison with observations on abundances of SN remnants

Recently, Kimura (2009); Uchida et al. (2009) have analyzed the metal distribution of the Cygnus loop by using the

data obtained by the Suzaku and XMM-Newton observations. It is pointed out that the progenitor of the Cygnus loop is a core-collapse supernova explosion whose progenitor mass ranges in  $\sim 12\text{--}15M_{\odot}$ . The ejecta distributions are asymmetric to the geometric center: the ejecta of O, Ne are distributed more in the north-west rim, while the ejecta of Si and Fe are distributed more in the south-west of the Cygnus loop. Since the material in this middle-aged supernova remnant has not been completely mixed yet, the observed asymmetry is considered to still remain a trace of inhomogeneity produced at the moment of explosion. These evidences may allow us to speculate that the asymmetry of the heavy element observed in the Cygnus loop may come from globally asymmetric explosions explored in this work. We try to seek the relevance in the following.

Figure 17 shows number ratios of Ne, Mg, Si, and Fe relative to O observed in Cygnus loop and those of ejecta for  $L_{\nu_e} = 4.5 \times 10^{52} \text{ erg s}^{-1}$ . We find that the ratios observed in Cygnus loop (solid line) are comparable to those averaged over ejecta from the inner lower region ( $r_{\text{ej,cc}} \leq 10,000 \text{ km}$  and  $\theta \geq 2\pi/3$ ) (dotted line). The ratios averaged over all the ejecta (dash-dotted line) are same as those averaged over ejecta from the inner equatorial region ( $r_{\text{ej,cc}} \leq 10,000 \text{ km}$  and  $\pi/3 < \theta < 2\pi/3$ ) (dashed line). We note that the ratios averaged over the ejecta from the inner upper region ( $r_{\text{ej,cc}} \leq 10,000 \text{ km}$  and  $\theta \leq \pi/3$ ) are comparable to but slightly lower than those averaged over the ejecta from the inner lower region (dotted line).

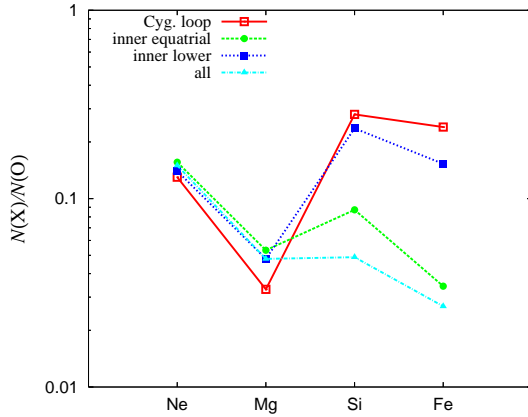


FIG. 17.— Number ratios of Ne, Mg, Si, and Fe relative to O observed in Cygnus loop and those of ejecta for  $L_{\nu_e} = 4.5 \times 10^{52} \text{ erg s}^{-1}$  at  $t = 1.5 \text{ s}$ . Solid line indicates ratios observed in Cygnus loop, while dotted, dashed, and dash-dotted line indicate ratios averaged over ejecta from an inner equatorial region ( $r_{\text{ej,cc}} \leq 10,000 \text{ km}$  and  $\pi/3 < \theta < 2\pi/3$ ), ejecta from an inner polar region ( $r_{\text{ej,cc}} \leq 10,000 \text{ km}$  and  $\theta \geq 2\pi/3$ ), and all the ejecta, respectively.

$N(\text{Ne})/N(\text{O})$  and  $N(\text{Mg})/N(\text{O})$  are independent from an averaging region and are comparable to all our aspherical models. These ratios are therefore concluded to be determined during the hydrostatic evolution of the progenitor and thus are a good indicator for the progenitor mass. On the other hand, ratios of Si and Fe relative to O are much higher in the inner region, in particular in the inner lower region, compared with the outer region ( $\geq 10,000 \text{ km}$ ).  $N(\text{Si})/N(\text{O})$  and  $N(\text{Fe})/N(\text{O})$  averaged over all the ejecta are much smaller than those observed in Cygnus loop. Therefore incomplete radial mixing of Fe and Si with O is required to be explained the high Fe and Si ratios in Cygnus loop. In fact, the averaged abundances of the Cygnus loop have a correlation with the Si- and Fe- rich re-

gions (Kimura 2009; Uchida et al. 2009). Our results suggest that the abundance ratios for Ne and Mg as well as Si and Fe observed in the Cygnus loop could be well reproduced with the SN ejecta from the inner region of a  $15M_{\odot}$  progenitor.

#### 4.6. Three dimensional effects

In order to draw a robust conclusion to the findings obtained in the current 2D simulations, it is indispensable to move on to three dimensional (3D) simulations (e.g., Blondin & Mezzacappa (2007); Iwakami et al. (2008, 2009); Nordhaus et al. (2010); Wongwathanarat et al. (2010)). In 2D, the growth of SASI and the large-scale convection tend to develop along the coordinate symmetry axis preferentially, thus suppressing the anisotropies in explosions as well as in the resulting explosive nucleosynthesis. An encouraging news to us is that 3D simulations cited above are, at least, in favour of the SASI-aided low-modes explosions, in which the major axis of the expanding shock has a certain direction at the moment of explosion (albeit free from the coordinate symmetry axis). By incorporating the present scheme to the 3D simulations of Iwakami et al. (2008, 2009), we plan to clarify these issues as a sequel of this study.

### 5. SUMMARY

We have investigated the explosive nucleosynthesis in the delayed neutrino-driven, aspherical SN explosion aided by SASI, based on 2D, axisymmetric hydrodynamic simulations of the explosion of a non-rotating  $15M_{\odot}$  star. We employed a hydrodynamic code with a simplified light-bulb neutrino transport scheme. We have approximately taken into account neutrino heating and cooling as well as the evolution of electron fraction due to weak interactions, both in the hydrodynamic simulations and nucleosynthetic calculations. Neutrinos are assumed to be isotropically emitted from the neutrino spheres with given luminosities and with the Fermi-Dirac distribution of given temperatures. We have performed simulations with the temperatures and luminosities of  $\nu_e$ ,  $\bar{\nu}_e$  and  $\nu_x$  constant in time. We have followed abundance evolution of SN ejecta using the nuclear reaction network coupled with an evolution equation of the electron fraction of the ejecta.

We summarize our results as follows,

1. The stalled shock revives due to the neutrino heating aided by SASI for cases with  $L_{\nu_e} \geq 3.9 \times 10^{52} \text{ erg s}^{-1}$  and the aspherical shock passes through the outer layers of the star ( $\geq 10,000 \text{ km}$ ). Evaluated explosion energies roughly correlate with neutrino luminosities. For models with larger luminosities, the explosion occurs earlier and mass of a neutron star becomes lighter.
2. Whole of the iron core of the progenitor collapses to the proto neutron star. The infall of material to the star is aspherical. Larger amounts of the gas infall from directions with lower explosion energies.
3. Abundances of the neutrino-heated ejecta are highly uncertain, in particular for neutron-rich ones, due to the uncertainty in the estimate on  $Y_e$ . On the other hand, the shock-heated ejecta has definite abundances, which depend on the maximum temperature mainly. The uncertainty in the estimate of the masses and abundances of abundant nuclei in the SN ejecta is small because of the small fraction of the neutrino-heated ejecta.

4. Abundance pattern of the supernova ejecta is similar to that of the solar system, for cases with the mass of the ejecta from the inner region ( $\leq 10,000$  km),  $M_{\text{ej, in}} = (0.4-0.5)M_{\odot}$ , which corresponds to models with a high explosion energy of  $\simeq 10^{51}$  erg. Masses of a neutron star remnant, estimated to be  $(1.54-1.62)M_{\odot}$  for these models, are comparable to the baryonic mass of the neutron star observed in neutron-star binaries.  $E_{\text{exp}}/M_{\text{ej}}$  evaluated for the models  $((0.92-1.2) \times 10^{50} \text{ erg}/M_{\odot})$  are comparable to the estimate in SN 1987A.
5. Underproduction of  $^{44}\text{Ti}$  and overproduction of  $^{62}\text{Ni}$ , which appear in spherical models, are also shown in our 2D calculations. The overproduction of  $^{62}\text{Ni}$  possibly inherits the uncertainty not only in the progenitor model but also of the change in  $Y_e$  during the SN explosion. On the other hand,  $^{64}\text{Zn}$ , which is underproduced in a spherical model, is found to be abundantly produced in our 2D model, although the abundance and mass are uncertain.
6. Distributions of nuclei and energy are highly aspherical in the SN ejecta, although the progenitor is non-rotating and has spherical symmetric configuration. The shock-heated ejecta forms aspherical and deformed shell-like structure composed of Fe, Si, and O from inside to out-

side. The neutrino-heated ejecta do not have any definite structure and fractions of the ejecta are mixed into the shell-like structure of the shock-heated ejecta.

7. The asymmetry of  $^{28}\text{Si}$  mass distribution is similar to that of the explosion energy and smaller than that of  $^{56}\text{Ni}$ .  $^{40}\text{Ca}$  and  $^{44}\text{Ti}$  are accompanied with  $^{28}\text{Si}$  and  $^{56}\text{Ni}$ , respectively.
8. The ratios for Ne, Mg, Si and Fe observed in Cygnus loop are well reproduced with the SN ejecta from the inner region of the  $15M_{\odot}$  progenitor. The number ratios for Ne and Mg relative to O seem to be good indicators for the mass of a progenitor of a core-collapse SN.

S.F. is grateful to K. Sumiyoshi for fruitful discussions. K.K. thanks to S. Nagataki for stimulating discussions and also thanks to K. Sato and S. Yamada for continuing encouragements. This work is partly supported by a grant for Basic Science Research Projects from the Sumitomo Foundation (No. 080933) and Grant-in-Aid for Scientific Research from the Ministry of Education, Culture, Sports, Science and Technology of Japan (Nos. 19540309, 20740150, 22540297).

## REFERENCES

- Anders, E., & Grevesse, N. 1989, *Geochim. Cosmochim. Acta* 53, 197
- Blinnikov, S. I., Dunina-Barkovskaya, N. V., & Nadyozhin, D. K. 1996, *ApJS*, 106, 171
- Borkowski, K. J., et al. 2010, arXiv:1006.3552, accepted for publication in *ApJL*
- Blondin, J. M., Mezzacappa, A., & DeMarino, C. 2003, *ApJ*, 584, 971
- Blondin, J. M., & Mezzacappa, A. 2007, *Nature*, 445, 58
- Buras, R., Janka, H.-T., Rampp, M., & Kifonidis, K. 2006, *A&A*, 457, 281
- Buras, R., Rampp, M., Janka, H.-T., & Kifonidis, K. 2006, *A&A*, 447, 1049
- Burrows, A., Young, T., Pinto, P., Eastman, R., & Thompson, T. A. 2000, *ApJ*, 539, 865
- Couch, S. M., Wheeler, J. C., & Milosavljević, M., 2009, *ApJ*, 696, 953
- Cybur, R. H., et al., 2010, *ApJS*, 189, 240
- Fischer, T., Whitehouse, S. C., Mezzacappa, A., Thielemann, F.-K., & Liebendörfer, M. 2010, *A&A*, 517, A80
- Foglizzo, T., Galletti, P., Scheck, L., & Janka, H.-T. 2007, *ApJ*, 654, 1006
- Fröhlich, C., et al. 2006, *ApJ*, 637, 415
- Fröhlich, C., et al. 2006, *Physical Review Letters*, 96, 142502
- Fujimoto, S., Hashimoto, M., Arai, K., & Matsuba, R. 2004, *ApJ*, 614, 817
- Fujimoto, S., Kotake, K., Yamada, S., Hashimoto, M., & Sato, K. 2006, *ApJ*, 644, 1040
- Fujimoto, S., Hashimoto, M., Kotake, K., & Yamada, S. 2007, *ApJ*, 656, 382
- Fujimoto, S., Nishimura, N., & Hashimoto, M. 2008, *ApJ*, 680, 1350
- Fuller, G. M., Fowler, W. A., & Newman, M. J. 1980, *ApJS*, 42, 447
- . 1982, *ApJS*, 48, 279
- Gawryszczak, A., Guzman, J., Plewa, T., & Kifonidis, K. 2010, *A&A*, 521, 38
- Goriely, S., Arnould, M., Borzov, I., & Rayet, M. 2001, *A&A*, 375, L35
- Hammer, N. J., Janka, H.-T., & Müller, E. 2010, *ApJ*, 714, 1371
- Hashimoto, M. 1995, *Prog. Theor. Phys.* 94 663.
- Haxton, W. C. 1988, *Phys. Rev. Lett.*, 60, 1999
- Hoffman, R. D., Woosley, S. E., Weaver, T. A., Timmes, F. X., Eastman, R. G., & Hartmann, D. H., 1995, *ApJ*, 759, 267
- Hoffman, R. D., et al., 2010, *ApJ*, 715, 1383
- Hughes, J. P., Rakowski, C. E., Burrows, D. N., & Slane, P. O. 2000, *ApJ*, 528, 109
- Hüdepohl, L., Müller, B., Janka, H.-T., Marek, A., & Raffelt, G. G. 2010, *Physical Review Letters*, 104, 251101
- Hungerford, A. L., Fryer, C. L., & Warren, M. S. 2003, *ApJ*, 594, 390
- Hungerford, A. L., Fryer, C. L., & Rockefeller, G. 2005, *ApJ*, 635, 487
- Iwakami, W., Kotake, K., Ohnishi, N., Yamada, S., & Sawada, K. 2008, *ApJ*, 678, 1207
- Iwakami, W., Kotake, K., Ohnishi, N., Yamada, S., & Sawada, K. 2009, *ApJ*, 700, 232
- Joggerst, C. C., Woosley, S. E., & Heger, A. 2009, *ApJ*, 693, 1780
- Joggerst, C. C., Almgren, A., Bell, J., Heger, A., Whalen, D., & Woosley, S. E. 2010, *ApJ*, 709, 11
- Kifonidis, K., Plewa, T., Janka, H.-T., Müller, E. 2003, *A&A*, 408, 621
- Kifonidis, K., Plewa, T., Scheck, L., Janka, H.-T., Müller, E. 2006, *A&A*, 453, 661
- Kitaura, F. S., Janka, H.-T., & Hillebrandt, W. 2006, *A&A*, 450, 345
- Kotake, K., Sawai, H., Yamada, S., & Sato, K. 2004, *ApJ*, 608, 391
- Marek, A., Janka, H.-T., & Müller, E. 2009, *A&A*, 496, 475
- Marek, A., & Janka, H.-T. 2009, *ApJ*, 694, 664
- Kimura, M., Tsunemi, H., Katsuda, S., & Uchida, H. 2009, *PASJ*, 61, 137
- Maeda, K., & Nomoto, K. 2003, *ApJ*, 598, 1163
- Maeda et al. 2008, *Science*, 319, 1220
- Modjaz, M., Kirshner, R. P., Blondin, S., Challis, P., & Matheson, T. 2008, *ApJ*, 687, 9
- Nagataki, S., Hashimoto, M., Sato, K., & Yamada, S. 1997, *ApJ*, 486, 1026
- Nagataki, S., 2000, *ApJS*, 127, 141
- Nagataki, S., Mizuta, A., & Sato, K. 2006, *ApJ*, 647, 1255
- Nakamura, S. X., Sumiyoshi, K., & Sato, T. 2009, *Phys. Rev. C*, 80, 035802
- Nishimura, S., Kotake, K., Hashimoto, M.-a., Yamada, S., Nishimura, N., Fujimoto, S., & Sato, K. 2006, *ApJ*, 642, 410
- Nordhaus, J., Burrows, A., Almgren, A., & Bell, J. 2010, *ApJ*, 720, 694
- Ohnishi, N., Kotake, K., & Yamada, S. 2006, *ApJ*, 641, 1018
- Ohnishi, N., Kotake, K., & Yamada, S. 2007, *ApJ*, 667, 375
- Ono, M., Hashimoto, M., Fujimoto, S., Kotake, K., & Yamada, S. 2009, *Progress of Theoretical Physics*, 122, 755
- Park, S., Hughes, J. P., Slane, P. O., Burrows, D. N., Gaensler, B. M., & Ghavamian, P. 2007, *ApJ*, 670, 121
- Pruet, J., Hoffman, R. D., Woosley, S. E., Janka, H.-T., & Buras, R. 2006, *ApJ*, 644, 1028
- Rauscher, T., Heger, A., Hoffman, R. D., & Woosley, S. E. 2002, *ApJ*, 576, 323
- Rayet, M., Arnould, M., Hashimoto, M., Prantzos, N., & Nomoto, K. 1995, *A&A*, 298, 517
- Renaud, M., et al. 2006, *ApJ*, 647, L41
- Ruffert, M., Janka, H.-T., & Schaefer, G. 1996, *A&A*, 311, 532
- Scheck, L., Plewa, T., Janka, H.-T., Kifonidis, K., Müller, E. 2004, *Physical Review Letters*, 92, 011103
- Scheck, L., Kifonidis, K., Janka, H.-T., & Müller, E. 2006, *A&A*, 457, 963
- Schwab, J., Podsiadlowski, P., & Rappaport, S. 2010, *ApJ*, 719, 722
- Seitenzahl, I. R., Röpke, F. K., Fink, M., & Pakmor, R. 2010, *MNRAS*, 407, 2297
- Shen, H., Toki, H., Oyamatsu, K., & Sumiyoshi, K. 1998, *Nucl. Phys. A.*, 637, 435
- Shigeyama, T., Nomoto, K., & Hashimoto, M. 1988, *A&A*, 196, 141
- Shigeyama, T., & Nomoto, K., 1990, *ApJ*, 360, 242
- Stone, J. M., & Norman, M. L. 1992, *ApJS*, 80, 791
- Suwa, Y., Kotake, K., Takiwaki, T., Whitehouse, S., & Liebendörfer, M. 2010, *PASJ*, 62, L49.
- Tanaka, M., Kawabata, K. S., Maeda, K., Hattori, T., & Nomoto, K. 2008, *ApJ*, 689, 1191
- Tanaka, M., et al. 2009a, *ApJ*, 699, 1119
- Tanaka, M., et al. 2009b, *ApJ*, 700, 1680
- Taubenberger, S. et al. 2009, *MNRAS*, 397, 677
- Thielemann, F.-K., Nomoto, K., & Hashimoto, M.-A. 1996, *ApJ*, 460, 408

Thielemann, F.-K., Rauscher, T., Freiburghaus, C., Nomoto, K., Hashimoto, M., Pfeiffer, B., & Kratz, K.-L. 1998, *Neutrino Physics and Astrophysics*, 27  
 Tominaga, N. 2009, *ApJ*, 690, 526  
 Uchida, H., Tsunemi, H., Katsuda, S., Kimura, M., & Kosugi, H. 2009, *PASJ*, 61, 301  
 Wanajo, S. 2006, *ApJ*, 647, 1323  
 Wanajo, S., Nomoto, K., Janka, H.-T., Kitaura, F. S., Müller, B. 2009, *ApJ*, 695, 208  
 Wang, L., et al., 2002, *ApJ*, 579, 671  
 Willingale, R., Bleeker, J. A. M., vanderHeyden, K. J., Kaastra, J. S., & Vink, J. 2002, *A&A*, 381, 1039

Wongwathanarat, A., Janka, H.-T., Müller, E. 2010, *ApJ*, 725, L106  
 Woosley, S. E. 1988, *ApJ*, 330, 218  
 Woosley, S. E., Hartmann, D. H., Hoffman, R. D., & Haxton, W. C., 1990, *ApJ*, 356, 272  
 Woosley, S. E., & Weaver, T. A. 1995, *ApJS*, 101, 181  
 Yoshida, T., et al., 2008, *ApJ*, 686, 448  
 Young, P. A., et al., 2006, *ApJ*, 640, 891  
 Young, P. A., & Fryer, C. L. 2007, *ApJ*, 664, 1033

## APPENDIX

In this appendix, we summarize our treatment on the rate of change in  $Y_e$  and energy per unit volume,  $Q_N$  and  $Q_E$ , respectively. We take into account absorption of electron and anti-electron neutrinos as well as neutrino emission through electron and positron captures, electron-positron pair annihilation, nucleon-nucleon bremsstrahlung, and plasmon-decays. Moreover, we include the heating term in  $Q_E$  due to the absorption of neutrinos on  $^4\text{He}$  and the inelastic scatterings on  $^4\text{He}$  via neutral currents (Haxton 1988; Ohnishi et al. 2007). We chiefly follow the treatments in Appendix D of Scheck et al. (2006) and in Appendix B of Ruffert et al. (1996) (and references therein).

### THE RATE OF CHANGE IN SPECIFIC ENERGY, $Q_E$

#### *neutrino absorption processes*

The heating rate per unit volume through the absorption of  $\nu_e$  on neutrons is described as

$$Q_{\nu_e}^a = \sigma c \frac{L_{\nu_e} n_n}{4\pi r^2 c f_{\nu_e}} \frac{\langle \epsilon_{\nu_e}^3 \rangle + 2\Delta \langle \epsilon_{\nu_e}^2 \rangle + \Delta^2 \langle \epsilon_{\nu_e} \rangle}{\langle \epsilon_{\nu_e} \rangle} \Theta(\langle \epsilon_{\nu_e} \rangle), \quad (\text{A1})$$

where  $\Delta = (m_n - m_p)c^2$ ,  $n_n$  is the number density of neutrons, and  $\sigma = 4G_F^2 m_e^2 \hbar^2 / \pi c^2 = \frac{1}{4}(3\alpha_w^2 + 1)\sigma_0 / (m_e c^2)^2$ , with the Fermi coupling constant  $G_F$ , the reduced planck constant  $\hbar$ , the electron mass  $m_e$ ,  $\alpha_w = 1.254$ , and  $\sigma_0 = 1.76 \times 10^{-44} \text{ cm}^2$ . Here, the  $n$ -th energy moment of  $\nu_e$ ,  $\langle \epsilon_{\nu_e}^n \rangle$ , is given by

$$\langle \epsilon_{\nu_i}^n \rangle = (k_B T_{\nu_i})^n \frac{\mathcal{F}_{2+n}(\eta_{\nu_i})}{\mathcal{F}_2(\eta_{\nu_i})}, \quad (\text{A2})$$

and a factor for the Pauli blocking,  $\Theta(\langle \epsilon_{\nu_i} \rangle)$ , is approximated as

$$\Theta(\langle \epsilon_{\nu_i} \rangle) = 1 - f_{\text{FD}} \left( \frac{\langle \epsilon_{\nu_i} \rangle + \Delta}{k_B T}, \eta_{e^-} \right), \quad (\text{A3})$$

where  $\eta_{\nu_i}$  is the chemical potential of  $\nu_i$  in units of  $k_B T$  and set to be 0,  $\eta_{e^-}$  is the chemical potential of electrons in units of  $k_B T$ ,  $k_B$  is the Boltzmann constant, and  $\mathcal{F}_n(\eta)$  is defined as,

$$\mathcal{F}_n(\eta) \equiv \int_0^\infty dx x^n f_{\text{FD}}(x, \eta) \quad (\text{A4})$$

using the Fermi-Dirac distribution function,

$$f_{\text{FD}}(x, \eta) = \frac{1}{1 + \exp(x - \eta)}. \quad (\text{A5})$$

The heating rate via the absorption of  $\bar{\nu}_e$  on protons is given by

$$Q_{\bar{\nu}_e}^a = \sigma c \frac{L_{\bar{\nu}_e} n_p}{4\pi r^2 c f_{\bar{\nu}_e}} \frac{\langle \epsilon_{\bar{\nu}_e}^3 \rangle^* + 3\Delta \langle \epsilon_{\bar{\nu}_e}^2 \rangle^* + 3\Delta^2 \langle \epsilon_{\bar{\nu}_e} \rangle^* + \Delta^3 \langle \epsilon_{\bar{\nu}_e}^0 \rangle^*}{\langle \epsilon_{\bar{\nu}_e} \rangle}, \quad (\text{A6})$$

where the  $n$ -th energy moment of  $\bar{\nu}_e$ ,  $\langle \epsilon_{\bar{\nu}_e}^n \rangle^*$ , is given by

$$\langle \epsilon_{\bar{\nu}_i}^n \rangle^* = (k_B T_{\bar{\nu}_i})^n \frac{\mathcal{F}_{2+n}(\eta_{\bar{\nu}_i} - \Delta / k_B T_{\bar{\nu}_i})}{\mathcal{F}_2(\eta_{\bar{\nu}_i})}. \quad (\text{A7})$$

#### *Capture processes*

The energy emission rate of  $\nu_e$  per unit volume via electron capture on protons is given by

$$Q_{\nu_e}^e = \frac{\sigma c}{2} n_p n_{e^-} [\langle \epsilon_{e^-}^3 \rangle^* + 2\Delta \langle \epsilon_{e^-}^2 \rangle^* + \Delta^2 \langle \epsilon_{e^-} \rangle^*], \quad (\text{A8})$$

and that of  $\bar{\nu}_e$  via positron capture on neutrons by

$$Q_{\bar{\nu}_e}^e = \frac{\sigma c}{2} n_n n_{e^+} [\langle \epsilon_{e^+}^3 \rangle + 3\Delta \langle \epsilon_{e^+}^2 \rangle + 3\Delta^2 \langle \epsilon_{e^+} \rangle + \Delta^3]. \quad (\text{A9})$$

Here, the number densities of electrons and positrons are described by

$$n_{e^\mp} = \frac{8\pi}{(hc)^3} (k_B T)^3 \mathcal{F}_2(\pm \eta_{e^\mp}), \quad (\text{A10})$$



where  $h$  is the Planck constant, and the  $n$ -th energy moments of electrons and positrons,  $\langle \epsilon_e^n \rangle$  and  $\langle \epsilon_e^n \rangle^*$ , are given by

$$\langle \epsilon_e^n \rangle = (k_B T)^n \frac{\mathcal{F}_{2+n}(\eta_e)}{\mathcal{F}_2(\eta_e)} \quad (\text{A11})$$

and

$$\langle \epsilon_e^n \rangle^* = (k_B T)^n \frac{\mathcal{F}_{2+n}(\eta_e - \Delta/k_B T)}{\mathcal{F}_2(\eta_e)}. \quad (\text{A12})$$

#### Pair processes

The energy emission rates of  $\nu_e$  and  $\bar{\nu}_e$  per unit volume via electron-positron pair annihilations are given by

$$\mathcal{Q}_{\nu_e}^{\text{pa}} = \mathcal{Q}_{\bar{\nu}_e}^{\text{pa}} = \frac{C_V^2 + C_A^2}{36} \left( \frac{8\pi}{(hc)^3} \right)^2 \frac{\sigma_0 c}{(m_e c^2)^2} (k_B T)^9 [\mathcal{F}_4(\eta_e) \mathcal{F}_3(-\eta_e) + \mathcal{F}_3(\eta_e) \mathcal{F}_4(-\eta_e)] P_{\text{pair}, \nu_e} P_{\text{pair}, \bar{\nu}_e}, \quad (\text{A13})$$

where  $C_A = \frac{1}{2}$ ,  $C_V = \frac{1}{2} + 2 \sin^2 \theta_W$ , and  $\sin^2 \theta_W = 0.23$ . Here  $P_{\text{pair}, \nu_e}$  and  $P_{\text{pair}, \bar{\nu}_e}$  are factors for the phase space blocking of  $\nu_e$  and  $\bar{\nu}_e$  for the pair processes, respectively and the factor for  $\nu_i$  is approximately expressed as

$$P_{\text{pair}, \nu_i} \simeq \left\{ 1 + \exp \left[ - \left( \frac{1}{2} \frac{\mathcal{F}_4(\eta_e)}{\mathcal{F}_3(\eta_e)} + \frac{1}{2} \frac{\mathcal{F}_4(-\eta_e)}{\mathcal{F}_3(-\eta_e)} - \eta_{\nu_i} \right) \right] \right\}^{-1}. \quad (\text{A14})$$

The energy emission rate of  $\nu_x$  per unit volume via the pair annihilations is given by

$$\mathcal{Q}_{\nu_x}^{\text{pa}} = \frac{(C_V - C_A)^2 + (C_V + C_A - 2)^2}{18} \left( \frac{8\pi}{(hc)^3} \right)^2 \frac{\sigma_0 c}{(m_e c^2)^2} (k_B T)^9 [\mathcal{F}_4(\eta_e) \mathcal{F}_3(-\eta_e) + \mathcal{F}_3(\eta_e) \mathcal{F}_4(-\eta_e)] (P_{\text{pair}, \nu_x})^2. \quad (\text{A15})$$

#### Nucleon-nucleon bremsstrahlung processes

The energy emission rate per unit volume through nucleon-nucleon bremsstrahlung of a single neutrino pair is well approximated with

$$\mathcal{Q}_{\nu\bar{\nu}}^{\text{br}} = 1.04 \times 10^{30} \zeta (X_n^2 + X_p^2 + \frac{28}{3} X_n X_p) \left( \frac{\rho}{10^{14} \text{ g cm}^{-3}} \right)^2 \left( \frac{T}{1 \text{ MeV}} \right)^{5.5} \text{ erg cm}^{-3} \text{ s}^{-1}, \quad (\text{A16})$$

where  $\zeta$  is set to be 0.5 (Burrows et al. 2000), and  $X_n$  and  $X_p$  are the mass fraction of neutrons and protons, respectively.

#### Plasmon decay processes

The emission rates of  $\nu_e$  and  $\bar{\nu}_e$  per unit volume via plasmon decay are given by

$$R_{\nu_e}^{\text{pl}} = R_{\bar{\nu}_e}^{\text{pl}} = C_V^2 \frac{\pi^3}{3\alpha_* (hc)^6} \frac{\sigma_0 c}{(m_e c^2)^2} (k_B T)^8 \gamma^6 e^{-\gamma} (1 + \gamma) P_{\text{plas}, \nu_e} P_{\text{plas}, \bar{\nu}_e}, \quad (\text{A17})$$

where  $\alpha_* = 1/137.036$  is the fine-structure constant,  $\gamma = \gamma_0 \sqrt{\eta_e^2 + \pi^2/3}$  with  $\gamma_0 = 2\sqrt{\alpha_*/3\pi} = 5.565 \times 10^{-2}$ ,  $P_{\text{plas}, \nu_e}$  and  $P_{\text{plas}, \bar{\nu}_e}$  are factors for the phase space blocking of  $\nu_e$  and  $\bar{\nu}_e$  for plasmon decay processes, respectively. The factor for  $\nu_i$  is approximately expressed as

$$P_{\text{plas}, \nu_i} \simeq \left\{ 1 + \exp \left[ - \left( 1 + \frac{1}{2} \frac{\gamma^2}{1 + \gamma} - \eta_{\nu_i} \right) \right] \right\}^{-1}. \quad (\text{A18})$$

The emission rate of  $\nu_x$  per unit volume via plasmon decay is given by

$$R_{\nu_x}^{\text{pl}} = (C_V - 1)^2 \frac{4\pi^3}{3\alpha_* (hc)^6} \frac{\sigma_0 c}{(m_e c^2)^2} (k_B T)^8 \gamma^6 e^{-\gamma} (1 + \gamma) (P_{\text{plas}, \nu_x})^2 \quad (\text{A19})$$

The energy emission rates of  $\nu_i$  per unit volume via plasmon decay is given by

$$\mathcal{Q}_{\nu_i}^{\text{pl}} = R_{\nu_i}^{\text{pl}} \cdot k_B T \left( 1 + \frac{1}{2} \frac{\gamma^2}{1 + \gamma} \right) \quad (\text{A20})$$

#### Neutrino absorption on helium and inelastic neutrino-helium scatterings

In addition to the heating processes through the neutrino absorption on nucleons, the heating processes due to neutrino-helium interactions are taken into account, as in Ohnishi et al. (2007). Through the absorption of  $\nu_e$  and  $\bar{\nu}_e$  and the neutrino-helium inelastic scatterings on nuclei via neutral currents,  $\nu + (A, Z) \rightarrow \nu + (A, Z)^*$ , the heating rate per unit volume,  $\mathcal{Q}^\alpha$ , is evaluated as

$$\begin{aligned} \mathcal{Q}^\alpha = & \frac{\rho X_A}{m_B} \frac{31.6 \text{ MeV}}{(r/10^7 \text{ cm})^2} \left[ \frac{L_{\nu_e}}{10^{52} \text{ ergs s}^{-1}} \left( \frac{5 \text{ MeV}}{T_{\nu_e}} \right) \frac{A^{-1} \langle \sigma_{\nu_e}^+ E_{\nu_e} + \sigma_{\nu_e}^0 E_{\text{ex}}^A \rangle_{T_{\nu_e}}}{10^{-40} \text{ cm}^2 \text{ MeV}} \right. \\ & + \frac{L_{\bar{\nu}_e}}{10^{52} \text{ ergs s}^{-1}} \left( \frac{5 \text{ MeV}}{T_{\bar{\nu}_e}} \right) \frac{A^{-1} \langle \sigma_{\bar{\nu}_e}^- E_{\nu_e} + \sigma_{\bar{\nu}_e}^0 E_{\text{ex}}^A \rangle_{T_{\bar{\nu}_e}}}{10^{-40} \text{ cm}^2 \text{ MeV}} \\ & \left. + \frac{L_{\nu_x}}{10^{52} \text{ ergs s}^{-1}} \left( \frac{10 \text{ MeV}}{T_{\nu_x}} \right) \frac{A^{-1} \langle \sigma_{\nu_x}^0 E_{\text{ex}}^A + \sigma_{\bar{\nu}_x}^0 E_{\text{ex}}^A \rangle_{T_{\nu_x}}}{10^{-40} \text{ cm}^2 \text{ MeV}} \right], \quad (\text{A21}) \end{aligned}$$

where  $X_A$  is the mass fraction of the nucleus and  $m_B$  is the atomic mass unit (Haxton 1988). The last term denotes the sum of the contributions from  $\mu$  and  $\tau$  neutrinos. The cross section for each neutral-current is evaluated by the following fitting formula,

$$A^{-1} \langle \sigma_{\nu}^0 E_{\text{ex}}^A + \sigma_{\bar{\nu}}^0 E_{\text{ex}}^A \rangle_{T_{\nu}} = \alpha \left[ \frac{T_{\nu} - T_0}{10 \text{ MeV}} \right]^{\beta}, \quad (\text{A22})$$

where  $\alpha$ ,  $\beta$ , and  $T_0$  are given in Table I of Haxton (1988), and are chosen to be  $\alpha = 1.24 \times 10^{-40} \text{ MeV cm}^2$ ,  $\beta = 3.82$ , and  $T_0 = 2.54 \text{ MeV}$  (Ohnishi et al. 2007). In the first and second terms on the right hand side of Eq. (A21), the contributions from the charged current reactions,  $\sigma_{\nu}^+$  and  $\sigma_{\bar{\nu}}^-$ , are also taken into account according to Table II of Haxton (1988), that is,  $A^{-1} \langle \sigma_{\nu_e}^+ E_{\nu_e} \rangle_{T_{\nu_e}} = 0.30 \times 10^{-42} \text{ MeV cm}^2$  for  $T_{\nu_e} = 4 \text{ MeV}$  and  $A^{-1} \langle \sigma_{\bar{\nu}_e}^- E_{\bar{\nu}_e} \rangle_{T_{\bar{\nu}_e}} = 1.20 \times 10^{-42} \text{ MeV cm}^2$  for  $T_{\bar{\nu}_e} = 5 \text{ MeV}$ .

#### The rate of change in specific energy

The rate of change in energy in unit volume,  $Q_E$ , is evaluated as

$$Q_E = (Q_{\nu_e}^a + Q_{\bar{\nu}_e}^a) + Q^{\alpha} - (Q_{\nu_e}^c + Q_{\bar{\nu}_e}^c) - 3Q_{\nu\bar{\nu}}^{\text{br}} - (Q_{\nu_e}^{\text{pa}} + Q_{\bar{\nu}_e}^{\text{pa}} + 4Q_{\nu_x}^{\text{pa}}) - (Q_{\nu_e}^{\text{pl}} + Q_{\bar{\nu}_e}^{\text{pl}} + 4Q_{\nu_x}^{\text{pl}}), \quad (\text{A23})$$

where a factor of 3 in  $3Q_{\nu\bar{\nu}}^{\text{br}}$  corresponds three types of a neutrino pair  $\nu\bar{\nu}$ .

#### THE RATE OF CHANGE IN ELECTRON FRACTION, $Q_N$

The rate of change in  $Y_e$  per unit volume,  $Q_N$ , is evaluated as

$$Q_N = (\mathcal{R}_{\nu_e}^a - \mathcal{R}_{\bar{\nu}_e}^a - \mathcal{R}_{\nu_e}^c + \mathcal{R}_{\bar{\nu}_e}^c) \frac{m_B}{\rho}, \quad (\text{B1})$$

where  $\mathcal{R}_{\nu_e}^a$  and  $\mathcal{R}_{\bar{\nu}_e}^a$  are the absorption rates of  $\nu_e$  and  $\bar{\nu}_e$ , respectively, and  $\mathcal{R}_{\nu_e}^c$  and  $\mathcal{R}_{\bar{\nu}_e}^c$  are the emission rates of  $\nu_e$  and  $\bar{\nu}_e$  through the capture of electrons on protons and that of positron on neutrons, respectively. We ignore the variations of the electron fraction by the neutrino absorption on  $^4\text{He}$ , since they are minor and give no qualitative difference to the dynamics (Ohnishi et al. 2007).

The absorption rates of  $\nu_e$  and  $\bar{\nu}_e$  per baryon are computed as

$$\mathcal{R}_{\nu_e}^a = \sigma c \frac{L_{\nu_e} n_n}{4\pi r^2 c f_{\nu_e}} \frac{\langle \epsilon_{\nu_e}^2 \rangle + 2\Delta \langle \epsilon_{\nu_e} \rangle + \Delta^2}{\langle \epsilon_{\nu_e} \rangle} \Theta(\langle \epsilon_{\nu_e} \rangle), \quad (\text{B2})$$

and

$$\mathcal{R}_{\bar{\nu}_e}^a = \sigma c \frac{L_{\bar{\nu}_e} n_p}{4\pi r^2 c f_{\bar{\nu}_e}} \frac{\langle \epsilon_{\bar{\nu}_e}^2 \rangle^* + 2\Delta \langle \epsilon_{\bar{\nu}_e} \rangle^* + \Delta^2 \langle \epsilon_{\bar{\nu}_e}^0 \rangle^*}{\langle \epsilon_{\bar{\nu}_e} \rangle}, \quad (\text{B3})$$

respectively.

The emission rate of  $\nu_e$  per baryon through the electron capture on protons is given by

$$\mathcal{R}_{\nu_e}^c = \frac{1}{2} \sigma c n_p n_{e^-} [\langle \epsilon_{e^-}^2 \rangle^* + 2\Delta \langle \epsilon_{e^-} \rangle^* + \Delta^2 \langle \epsilon_{e^-}^0 \rangle^*] \quad (\text{B4})$$

and that of  $\bar{\nu}_e$  via the positron capture on neutrons by

$$\mathcal{R}_{\bar{\nu}_e}^c = \frac{1}{2} \sigma c n_n n_{e^+} [\langle \epsilon_{e^+}^2 \rangle + 2\Delta \langle \epsilon_{e^+} \rangle + \Delta^2]. \quad (\text{B5})$$